Fermi National Accelerator Laboratory

FERMILAB-Pub-79/81-EXP
7120.069

(Submitted to Phys. Rev.)

A HIGH STATISTICS STUDY OF $\pi^+ p$, $\pi^- p$, AND pp ELASTIC SCATTERING AT 200 GeV/c

A. Schiz, L. A. Fajardo, R. Majka, J. N. Marx,
P. Nemethy, L. Rosselet, J. Sandweiss, and A. J. Slaughter
Yale University, New Haven, Connecticut 06520

and

C. Ankenbrandt, M. Atac, R. Brown, S. Ecklund,
P. J. Gollon, J. Lach, J. MacLachlan, A. Roberts, and G. Shen
Fermi National Accelerator Laboratory, Batavia, Illinois 60510

December 1979

A HIGH STATISTICS STUDY OF π^+p, π^-p and pp ELASTIC SCATTERING AT 200 GeV/c

A. Schiz,[a] L. A. Fajardo, R. Majka,[b] J. N. Marx,[b] P. Nemethy,[b] L. Rosselet,[c] J. Sandweiss, and A. J. Slaughter
Yale University
New Haven, Connecticut 06520

and

C. Ankenbrandt, M. Atac, R. Brown,[d] S. Ecklund,[e] P. J. Gollon,[f] J. Lach, J. MacLachlan, A. Roberts, and G. Shen[g]
Fermi National Accelerator Laboratory
Batavia, Illinois 60510

ABSTRACT

We have measured π^-p, π^+p, and pp elastic scattering at an incident beam momentum of 200 GeV/c in the region of -t, four momentum transfer squared, from 0.021 to 0.665 $(GeV/c)^2$. The data allow an investigation of the t dependence of the logarithmic forward slope parameter, $b \equiv \frac{d}{dt}(\ln d\sigma/dt)$. In addition to standard parameterizations, we use functional forms suggested by the Additive Quark Model to fit the measured $d\sigma/dt$ distributions. Within the context of this model we estimate the size of the clothed quark in the pion and proton. Limits on the elastic scattering amplitude derived from unitarity bounds are checked, and no violations are observed.

INTRODUCTION

The distribution in t, four momentum transfer squared, for elastic scattering of hadrons provides information about the character of the strong interaction. In an optical model this distribution is dependent on the sizes and opacities of the interacting particles. The Additive Quark Model (AQM) derives $d\sigma/dt$ from a simple quark-quark interaction modified by form factors which reflect the spacial distribution of the quarks inside the interacting hadrons. In a Regge model this distribution depends on the structure of the Pomeron and of any other exchanges which contribute to elastic scattering.

Data from early experiments[1] at $-t < 0.8$ $(GeV/c)^2$ and at moderate energies (5 to 30 GeV) were fit with a simple exponential function of t:

$$\frac{d\sigma}{dt} = Ae^{bt} \qquad (1)$$

where b is independent of t. However later results from experiments at Fermilab,[2,3] SLAC,[4] and the ISR[5] show a more complicated t dependence of $d\sigma/dt$. An exponential with a quadratic term

$$\frac{d\sigma}{dt} = Ae^{bt + ct^2} \qquad (2)$$

gives a good representation of the Fermilab data taken with beam energies between 50 and 175 GeV in the intermediate t range ($0.05 < -t < 1.0$ $(GeV/c)^2$). Very precise data at 10 and 14 GeV from SLAC show an even more complicated t dependence, while the ISR results suggest a break in the t distribution for proton-proton scattering.

Finally data from the CERN SPS [6] on the logarithmic forward slope in the small t region ($-t < 0.05$ $(GeV/c)^2$) are inconsistent with extrapolated values of the slope as derived from data in the intermediate t range.

We have made a high statistics study of $\pi^- p$, $\pi^+ p$, and pp elastic scattering at 200 GeV/c incident momentum. The t range is from -0.021 to -0.665 $(GeV/c)^2$ (scattering angles from approximately 0.7 mrad to 4 mrad). Thus in a single experiment we measure $d\sigma/dt$ over the small to intermediate t region.

The high statistics allow us to make a detailed study of the shape of the elastic scattering t distributions. We will present the t dependence of b, the logarithmic slope parameter, defined as

$$b(t) \equiv \frac{d}{dt}(\ln \frac{d\sigma}{dt}) . \qquad (3)$$

In addition to standard parameterizations, we use functional forms suggested by the AQM to fit the measured $d\sigma/dt$ distributions. We also check limits on the elastic scattering amplitude derived from unitarity bounds.

APPARATUS

The experiment was performed in the M6 West beam line[7] in the Meson Lab at Fermilab. The apparatus, shown in Fig. 1, is a high resolution spectrometer which detects the forward particle. The apparatus is described in detail in Ref. 8; therefore this section will review only the salient features.

The beam line consisted of three stages, each having point to parallel to point focusing (only the latter two stages are shown in Fig. 1). The second focus was momentum dispersed; thus by placing a proportional wire chamber (PWC) with 1 mm wire spacing at the second focus, the incoming momentum was measured with a precision of 0.05% ($\Delta p/p;\sigma$), with a systematic uncertainty of ± 1%.

Four Cerenkov counters identified pions, kaons, and protons. From the Cerenkov pressure curves, we determined that the contamination of the pion and proton signals by kaons was less than 0.5% and 0.001% respectively. The small contamination of electrons and muons in the beam was tagged at the downstream end of the experiment.

The liquid hydrogen (LH_2) target, 52.7 cm in length, and the detectors to measure the scattering angle, were located downstream of the Cerenkov counters in the third stage of the beam. They were mounted on a large reinforced concrete block for stability. Beam defining scintillation counters, B1 and B2 and a veto, VH1, were located at the upstream end of the concrete block. Immediately downstream of the target were two scintillation

counters, VH2 and VH3, used to suppress unwanted scatters from target electrons and hadronic inelastic scatters. Two stations of high resolution, high pressure PWCs on either side of the LH_2 target (stations 1-4 in Fig. 1) measured the scattering angle. At each station a measurement was made of the trajectory's x (horizontal) and y (vertical) coordinates. In addition station 3 measured the u and v coordinates (rotated 45 and 135 degrees from the horizontal). The chambers had a 70 μm resolution (σ), and the resulting scattering angles were measured to 30 μrad (σ).

The spectrometer magnets used to determine the momentum of the scattered particle were two dipoles of the type used in the Fermilab main ring. The horizontal and vertical apertures were 10 cm and 5 cm respectively. Measurements of the integrated field length were made over the magnet aperture; these were uniform to 0.04%. A particle of the central momentum was bent 34 mrad in the horizontal plane.

A scintillation counter, V, was placed at the third focus, or veto plane, of the beam. Figure 2 shows the placement of this counter relative to the beam center and relative to the projection of the last spectrometer magnet onto the veto plane. Unscattered beam tracks and scatters with -t less than 0.01 $(GeV/c)^2$ were vetoed by this counter. The counter's shape was chosen to provide a relatively uniform angular acceptance.

At the end of the apparatus were a pair of PWCs with an effective wire spacing of 1 mm. Using these PWCs (station 6 in Fig. 1) in conjunction with stations 3 and 4, the outgoing momentum was measured to a precision of 0.1% ($\Delta p/p;\sigma$) relative to the central value of the momentum.

DATA ACQUISITION

The data collection logic consisted of a two level trigger. The first level used the various scintillation counters of the apparatus; the second used an analog device called the Hardware Focus Scatter Detector (HFSD).[3] An event satisfying both levels will be referred to as a SCATTER.

The first level of the trigger for a SCATTER consisted of requirements on the various scintillation counters in the experiment. The basic criteria were

1. reasonable incoming beam trajectory: $B1 \cdot B2 \cdot \overline{VH1}$ along with other beam defining counters in the second beam stage (not shown in Fig. 1),
2. proper particle identification by the Cerenkov counters,
3. no other incident particle detected within ± 400 nsec of the trigger,
4. the particle traversed the entire apparatus, and
5. no signal from the veto, V, at the beam third focus.

A second level of triggering was necessary since the first level trigger was dominated by beam halo. The HFSD provided the second level to the SCATTER trigger. This analog device performed two tests using the track coordinates as measured in the high resolution PWCs. Figure 3 schematically presents the two calculations. First the track, as extrapolated from the coordinates measured in the two high resolution PWCs upstream of

the target (stations A and B in Fig. 3), was required to intercept a preset beam window in the veto plane; This requirement was imposed in both the x and the y projections and eliminated beam halo. The other condition was that the data from the two upstream and the most downstream high resolution chambers did not represent a collinear track. This parallel test, was required in only one projection. The analog processor took about 5 μsec to make its decision.

Two additional trigger types were recorded along with the scattered events; in both the HFSD was not required. The first was a specified fraction of events satisfying the first level of the SCATTER trigger. These events, called PRscaled ACcepted eVenTs (PSACVT), were used to study the HFSD performance and any biases it may have introduced into the data; no such biases were found.

The second additional trigger, called BEAM, was a sample of incident beam particles. The basic requirements were a reasonable incoming trajectory (as defined for the SCATTER trigger) and proper particle identification by the Cerenkov counters. These triggers provided information for alignment and absolute normalization.

For each accepted trigger the online computer, a DEC PDP15/40,[10] recorded the following information on magnetic tape: 1) the wires activated for each PWC; 2) pulse height information from various scintillation counters and digitized results from the HFSD algorithms; 3) scintillation counter trigger information for each event. In addition, the online computer periodically recorded values of various phototube voltages and of resistors placed in the LH_2 target to monitor temperature. Finally computer scaler totals and bookkeeping information were recorded for each beam spill.

The data were accumulated over a two week period. The accelerator operated at 400 GeV with a repetition rate of 10 seconds and a 1 second spill time. The beam contained typically 5×10^5 particles per accelerator pulse. Approximately 400 triggers were recorded per second; out of these approximately 40 were BEAMs, approximately 10 PSACVTs, and the remainder SCATTERs. The relative fraction of events recorded involving a particular particle type was scaled to result in an apparatus live time of 60%.

DATA REDUCTION

We used the quantity q in the analysis where

$$q = \sqrt{-t} \simeq P_b \theta \tag{4a}$$

where

P_b = beam momentum

θ = scattering angle

and

$$\frac{d\sigma}{dq} = -2\sqrt{-t}\,\frac{d\sigma}{dt} \tag{4b}$$

There are two reasons for this choice. The first is that the resolution of the apparatus was constant in q, with a standard deviation of 6.0 MeV/c, making it natural to bin events according to q. The second reason is that $d\sigma/dq$ vs. q is a more slowly varying

function than $d\sigma/dt$ vs. t. Thus $d\sigma/dq$ populates the bins more uniformly, thereby reducing the sensitivity of the fitting procedure to the following effects: 1) integration of the cross section over the bin; 2) the migration of events from bin to bin due to resolution.

The data reduction process kept only events with unambiguous single tracks before and after the LH_2 target. This requirement had to be fulfilled by both SCATTER and BEAM events. Data summary tapes were produced which contained the relevant kinematic quantities (q, scattering vertex position, etc.) of each event; cuts were then applied to extract the elastic scattering signal. The alignment procedure used a subset of BEAM events that had one and only one hit (a set of activated contiguous wires) per PWC.

The target full and target empty q distributions were normalized, and then a target empty subtraction (a 1-2% effect in the lowest q bins and negligible elsewhere) was performed. The normalization was accomplished using those BEAM events that traversed the entire apparatus; thus there was no need to make any correction for absorption of scattered particles downstream of the target or for overall PWC inefficiencies.

The major cuts applied to extract the elastic signal are given in Table I. We found that approximately 20% of the π^+p and pp triggers and 15% of the π^-p triggers survived the cuts. Half the triggers were eliminated by track reconstruction cuts imposed on the hits in the PWCs. The rest of the rejected triggers failed one or more cuts on the kinematic quantities associated with the

scatter. The most important of these were the requirements that the scatter vertex occur in the region of LH_2 target, that the recoil mass squared be in the neighborhood of the mass of the proton squared, that scattered particles not be near the boundary of counter V at the third focus, and that the outgoing trajectory not pass through any inefficient regions of PWC station 4. (These inefficient regions were included in the Monte Carlo discussed below).

At this point the normalized data was corrected for the acceptance of the apparatus. A Monte Carlo program calculated the acceptance as function of q. Events were generated with the scattering vertex in the LH_2 target and a flat distribution in q, and then traced through the apparatus. The incident beam phase space was derived from actual incoming beam tracks. Multiple scattering of the particle was simulated at the appropriate places, and local PWC inefficiencies and the effects of resolution on the application of the cuts to the kinematic quantities were taken into account.

The geometric acceptance for the π^+p and pp data is shown in Fig. 4. The acceptance is particle independent for data taken at the same time. The acceptance for the π^-p data is similar in shape.

There were two effects not included in the Monte Carlo: 1) radiative effects; 2) contamination of the elastic signal by inelastic scatters. Both of these processes lead to t dependent corrections to the scattering distributions since they change the shape of the recoil mass squared distribution in a t dependent manner.

Using Sogard's[11] formalism for radiative corrections and taking into account the apparatus resolution, we calculated the correction for our cut on recoil mass squared. The measured differential cross section is corrected as follows:

$$\left(\frac{d\sigma}{dt}\right)_{\text{corrected}} = e^{\delta}\left(\frac{d\sigma}{dt}\right)_{\text{measured}} \qquad (5)$$

where Fig. 5 presents $(e^{\delta} - 1)$. The π^- correction is identical to that for the π^+ to one part in 10^4.

The correction due to inelastic scatters was found by fitting the recoil mass squared distribution associated with different bins of q to an elastic peak and a term representing the inelastic scattering contribution. Figure 6 presents the results of one such fit. The amount of contamination was derived for our recoil mass squared cut. The percentage of inelastic contamination as a function of q is given in Fig. 7; it is approximately 2% at the smallest scattering angles and increases to 6% for pions and to 9% for the protons at the larger angles. The error on this correction is 10% of its magnitude. The measured differential cross section is corrected for the inelastic contamination as follows:

$$\left(\frac{d\sigma}{dt}\right)_{\text{corrected}} = (1 - \alpha)\left(\frac{d\sigma}{dt}\right)_{\text{measured}} \qquad (6)$$

where α is the inelastic contamination.

We found that our final results are not very sensitive to these two corrections. Each applied separately causes the extracted local slopes (see the next section) to vary by less than one standard deviation. Note that these two corrections act in opposite directions.

The final correction applied to the data was to correct for plural nuclear scattering (double scattering) in the hydrogen target. A particle may scatter twice before exiting the hydrogen target. These two small angle scatters can simulate a large angle scatter and thus artificially increase the cross section at large t. Hence if a correction for this effect is not made, one will measure for the single scattering distribution a shallower slope than the actual slope.

To make the correction, the data was multiplied by P_s where

$$P_s = 1 + k \exp(b\, t/2)/b \qquad (7)$$

where $t < 0$ and

- b = $b(t=0)$ (10.9, 10.8, and 12.1 $(GeV/c)^{-2}$ for $\pi^- p$, $\pi^+ p$, and pp; see Table IV)
- k = $\Gamma\sigma_t^2/64\pi\hbar^2$
- σ_t = hadron-proton total cross section
- Γ = $N_A \rho\, x/A$
- N_A = Avogadro's number
- ρ = target density
- x = target length
- A = atomic weight of hydrogen

At $-t = 0.1$, 0.4, and 0.6 $(GeV/c)^2$ this correction is 0.3% 1.4%, and 4.1% respectively for πp elastic scattering and 0.7%, 4%, and 11% respectively for pp elastic scattering. The correction is accurate to ± 5%.

RESULTS

The $d\sigma/dt$ distribution is calculated using the following formula:

$$\frac{d\sigma}{dt} = \frac{N_s(q) \cdot e^{\cdot \delta}(1-\alpha)\ P_s}{2 \cdot q \cdot \Gamma \cdot \epsilon(q) \cdot \Delta \cdot I_o} \qquad (8)$$

where

$N_s(q)$ = number of scattered particles in each q bin that pass all cuts

I_o = number of incident beam particles

$\epsilon(q)$ = acceptance as function of q

Δ = q bin size

P_s, δ, α = correction parameters as defined in Eqns. 5, 6, and 7

Figures 8 to 10 show the resulting $d\sigma/dt$ distributions for $\pi^- p$, $\pi^+ p$, and pp elastic scattering; Table II gives the numerical values of the cross section in units of $mb/(GeV/c)^2$. The pp, $\pi^+ p$, and $\pi^- p$ distributions contain 1.16×10^6, 2.22×10^5, and 4.28×10^5 events respectively. The errors shown are statistical only; there is an uncertainty in the overall normalization of 4.0%. This uncertainty is due mainly to the statistical error involved in

our method of counting the number of incident beam particles. The data have not been corrected so as to extrapolate to the optical point.

By varying the cuts used to extract the elastic signal, we estimate the following t-dependent systematic error on the $d\sigma/dt$ distributions: 0.5% for $0.02 \leq -t \leq 0.20$ $(GeV/c)^2$, ± 1% for $0.20 < -t \leq 0.35$ $(GeV/c)^2$, ±2% for $0.35 < -t \leq 0.50$ $(GeV/c)^2$, and ±4% for $0.50 < -t \leq 0.67$ $(GeV/c)^2$.

The displayed and tabulated $d\sigma/dt$ distributions have been corrected for inelastic contamination, for radiative effects, and for plural nuclear scattering. Also the contribution due to Coulomb scattering (including the Coulomb - nuclear interference contribution) has been removed. Table III presents the parameters used for this subtraction. The Coulomb correction is negligible above $-t = 0.035$ $(GeV/c)^2$ and only slightly significant below. Making reasonable variations of the parameters listed in Table III changes the derived local slopes by less than one standard deviation.

Figures 8 to 10 show a comparison of the differential cross sections for some of the experiments[2,3,6,14] that have measured elastic scattering in the same kinematic region. Note that our data display high statistical accuracy and bridge a t range not covered by any other single experiment.

EXTRACTION OF THE LOCAL SLOPE PARAMETERS

In order to study in detail the shape of the $d\sigma/dt$ distribution, we fit over small regions of t using an exponential form. Thus in the limit of an infinitely small t region, we obtain the forward slope, b, as function of t using Eq. 3. To orient the reader, we present Fig. 11 which shows what might be expected in a b vs. t plot for some simple functional forms of $d\sigma/dt$.

In the analysis we subdivided the entire t range into 9 or 10 subregions and still maintained small errors on the measured local slopes. The fits were performed using a least squares minimization procedure; the program MINUIT[13] was employed. The fitting method was such that the values of $d\sigma/dt$ at the endpoint of the i^{th} subregion was constrained to coincide with that at the beginning point of $i+1^{th}$ subregion. This of course introduced correlations between the measured local slopes. When fits were performed without the above constraint, the values of the local slopes were within a standard deviation of the results from the constrained fits. The constrained fits merely reduced the statistical errors of the results.

To estimate the systematic error,[12] we derived the local slopes with a number of cut variations. For example, we changed the recoil mass squared cut, while keeping all other cuts the same. Our estimate of the systematic error on a particular local slope is the maximum range of the values of that local slope obtained with different sets of cuts.

Another source of systematic error was the ±1% uncertainty in the absolute value of the incident beam momentum. This contribution is included in the systematic errors presented in Table IV. Note that in some cases the total systematic error is significant when compared to the statistical error on the local slope.

We present in Fig. 12 and Table IV the results of this type of analysis. The errors shown in Fig. 12 include both the statistical and systematic contribution added in quadrature.

We also show on Fig. 12 the results of a fit of $d\sigma/dt$ over the full t range to a quadratic form (Eq. 2). Table V exhibits the values of b and c derived from these fits.

By integrating the $d\sigma/dt$ distributions over t, we derived the total elastic cross sections. To calculate the contributions of the regions in t we did not directly measure, we used the results of the fits from which the local slopes were obtained. We found that when we extrapolated the $d\sigma/dt$ distributions to t=0, we were consistent within our experimental errors with the optical point. Therefore we normalized $d\sigma/dt$ to the optical point when we calculated the total elastic cross sections. Table VI presents the total elastic cross sections and the ratio of the total elastic cross section to the total cross section. The errors in Table VI include, in addition to the statistical uncertainties, the systematic uncertainties due to our extrapolation of the measured $d\sigma/dt$ distributions over unmeasured t regions. Our results are in good agreement with Akerlof et al[3] but in poor agreement with the statistically more precise data of Ayres et al[2]. We attribute this difference to our incorporation of the slope changes in the forward direction.

DISCUSSION

The data presented in Fig. 12 clearly demonstrate that the elastic scattering differential cross sections for the $\pi^{\pm}p$, and pp reactions at 200 GeV/c are not consistent with a simple exponential e^{bt}. For pp scattering the behavior is poorly parameterized by an exponential with a quadratic term $e^{bt + ct^2}$ (see Table V). However for $\pi^{\pm}p$ scattering, this form describes the t distributions for $-t \gtrsim 0.04$ $(GeV/c)^2$.

The local slope in the pp case decreases with increasing t in the region of $0.03 < -t < 0.25$ $(GeV/c)^2$. From $0.25 < -t < 0.65$ $(GeV/c)^2$ the local slope has a constant value of approximately 9.5 $(GeV/c)^{-2}$.

For the pions, in the region $0.10 < -t < 0.60$ $(GeV/c)^2$ the local slope decreases with increasing t. From $0.03 < -t < 0.10$ $(GeV/c)^2$ the local slope is relatively flat; finally there is a sharp increase in the value in the region $0.02 < -t < 0.03$ $(GeV/c)^2$.

Figure 12 suggests that in the region of $0.25 \leq -t \leq 0.60$ $(GeV/c)^2$ the dependence of the local slopes as a function of t is different for protons and pions. While we believe our results suggest the above, the data do not have sufficient statistical accuracy to conclusively demonstrate this supposition. We formed the ratio $R^{\pm}$ where

$$R^{\pm} = \frac{d\sigma/dt(pp)}{d\sigma/dt(\pi^{\pm}p)} \qquad (9)$$

and fit the ratio to the form Ce^{dt}. Table VII presents the fit

results. An exponential describes the general behavior of $R^{\pm}$ (for the π^- case there is no one region of -t that give a large contribution to the χ^2) which would indicate similar $d\sigma/dt$ shapes for the protons and pions. Also the value of d is in good agreement with what was found at 175 GeV/c by Ref. 2. To definitively settle the question approximately four times our present statistics in the region of $0.30 \lesssim -t \lesssim 0.60$ $(GeV/c)^2$ is required.

Figure 13 compares our measured local slopes with those measured by others [2, 3, 5, 6, 15, 16]. It should be noted that these other measurements of the forward slopes are derived from fits over much larger ranges of t than we used. This is especially true for references 2 and 3, where fits to a quadratic form were performed over their full t range (-0.02 to -0.40 for Ref. 2; -0.07 to -0.80 for Ref. 3) From the fit results, the forward slope at t equal to -0.20 $(GeV/c)^2$ is computed. It is seen that there is good agreement between all the experiments. The results from references 6 and 17 support our observation of a sharp increase in the local slope for the very small t range in π^-p scattering.

An analysis similar to ours has been performed for hadron-proton elastic scattering at energies of 10.4 and 14 GeV. It was found that the $\pi^{\pm}p$ and pp scattering exhibit a behavior more complicated than a simple exponential in t.

COMPARISONS OF THE DATA WITH THEORETICAL MODELS

Theoretical Models such as that of Chou and Yang [18] and versions of the AQM [19, 20] attribute the major part of the small t elastic cross section variation to the hadronic form factors of the target and the projectile. These form factors are assumed to be the same as the electromagnetic form factors. In the AQM the form factors describe the spatial distribution of the clothed quarks; in the very small t region, the scattering is dominated by single quark-quark scattering. In both these models the differential elastic cross section is given to first order as

$$d\sigma/dt = AF_t^2(t)F_p^2(t)\left|A_{qq}(t)\right|^2 \qquad (10)$$

where

A	$= N_o\sigma_t^2/16\ \pi\hbar^2$
N_o	= normalization factor
σ_t	= total cross section
$F_t(t)$	= hadronic form factor of the target
$F_p(t)$	= hadronic form factor of the projectile
$A_{qq}(t)$	= quark-quark scattering matrix element

In our analysis we assume the conventional dipole form for the proton form factor and the single pole form for the pion.

$$F_p(t) = \left[1 - r_p^2 t/(12\hbar^2)\right]^{-2}$$

$$F_\pi(t) = \left[1 - r_\pi^2 t/(6\hbar^2)\right]^{-1}$$

where

r_p = proton electromagnetic charge radius

r_π = pion electromagnetic charge radius

We have fit our $d\sigma/dt$ distributions to Eq. 10 using the following two forms for $A_{qq}(t)$:

$$|A_{qq}(t)|^2 = (1 + ut/2)^2, \text{ quadratic form} \qquad (11a)$$

$$|A_{qq}(t)|^2 = \exp(ut), \text{ exponential form} \qquad (11b)$$

The quadratic form is purely phenomenological; the exponential form is suggested by Bialas et al.[19] and Levin and Shekhter.[20] For the case of the exponential form (Eq. 11b) one can identify u with the quark radius, r_q, where[21]

$$r_q^2 = -2\hbar^2 u \qquad (12)$$

Note that in the Chou-Yang model, $A_{qq}(t)$ is unity.

The results of the fits are given in Tables VIII and IX. In some cases the fitted parameters are highly correlated.

The data are well represented over the full t range ($0.025 < -t < 0.620$ $(GeV/c)^2$ by Eq. 10 with the quadratic form for the quark-quark scattering matrix element (Eq. 11a). The fitted values of r_p and r_π are in remarkably good agreement with measured proton[21] and pion[22] electromagnetic charge radii. These fits give $u/2 = .80(GeV/c)^2$: thus the quadratic expression goes to zero at $-t = 1.2(GeV/c)^2$. This is close to the dip at $-t \sim 1.5$ $(GeV/c)^2$ seen by Akerlof et al.[3] in their 200 GeV/c pp cross section.

The fits using the exponential form for the matrix element (Table IX) were made using the full t range and a restricted t range ($0.025 < -t < 0.320$ $(GeV/c)^2$). Over the restricted t range, reasonable fits to the data were obtained. Over the full range the fits are somewhat poorer, and the value of r_p is about 10% lower than measurements of the proton electromagnetic charge radius.

Within the context of the above picture, one expects that the proton electromagnetic charge radius to be the same whether extracted from the $\pi^{\pm}p$ data or from the pp data and similarly for the pion electromagnetic charge radius whether extracted from the π^+p or π^-p data. Therefore we fit the π^-p, π^+p, and pp data simultaneously using a single r_π and r_p; in some fits the r_q's were required to be equal, in some the r_q's were allowed to vary independently. Fitting to the π^-p, π^+p, and pp data simultaneously

also reduced the correlation between the fitted parameters. As the exponential form of the matrix element (Eq. 11b) has physical motivation, only the results of the fits using this form are presented in Table X. Figure 14 shows the results using an exponential matrix element and fitting the data over the region $0.025 \leq -t \leq 0.320$ $(GeV/c)^2$.

We note from Table X that the fit to the data over the full t range allowing the r_q's to vary independently is reasonable and would indicate $r_q^p > r_q^\pi$. The fit constraining the quark radii to be the same in the proton and pion exhibit a somewhat poorer fit. In both cases the values of r_p are about 5% low when compared to measurements of the proton electromagnetic charge radius.

Over the region $0.025 < -t < 0.320$ $(GeV/c)^2$ the data are well represented by the fits using the exponential matrix element. This conclusion is true whether the r_q's are constrained to be equal or are allowed to vary independently (though with independent r_q's the fit is slightly improved). Again r_p is approximately 5% low when compared to measurements of the proton electromagnetic charge radius.

We are impressed with the general qualitative agreement of our $\pi^\pm p$ and pp elastic scattering data and the AQM. Our fit results show that the shape of $d\sigma/dt$ in the region $0.025 < -t < 0.620$ $(GeV/c)^2$ is described by a product of the electromagnetic form factors of the projectile and the target and a simple matrix element. This is especially true in the region $0.025 < -t < 0.320$ $(GeV/c)^2$. The fitted values for r_p and r_π are remarkably close to

their electromagnetic counterparts. Within the context of the AQM this is evidence that the hadronic form factors of the pion and proton are very similar to their electromagnetic form factors. The fitted value of the clothed quark radius is correlated with r_p and r_π but seems to be between 0.35 and 0.45 fm.

We do not claim that our analysis tests the above theoretical ideas in a strict sense. First Eq. 10 represents only the first order form for $d\sigma/dt$; higher order terms have been neglected. Also there are technical difficulties with the fitting procedure since the results are very sensitive to the values of the proton and pion electromagnetic charge radii. For example constraining r_p to be 0.81 fm causes the fit to the pp data using an exponential matrix element to be quite poor. Thus the uncertainty in the published values of the proton and especially the pion electromagnetic radii are a serious obstacle in further tests of the AQM as applied to high statistics elastic scattering data.

TESTS OF UNITARITY BOUNDS

Upper limits on the ratio of the scattering amplitude at a given t to the scattering amplitude at t = 0 can be derived. These limits assume unitarity and analyticity of the scattering amplitude in the complex s-plane (s = center of mass energy). Figure 15 shows how our data compare to one such upper bound, Eq. 1.3 of Ref. 24. It is seen that there is no violation of the bounds; however the data are close to saturating them. This behavior has also been observed at energies of 20-30 GeV.[23]

S. M. Roy [26] derives the following bound on dσ/dt for pion-nucleon elastic scattering:

$$b(t)\left(\left.\frac{d\sigma}{dt}\right|_t\right)^{1/2} \geq \frac{b(0)}{2}\left(\left.\frac{d\sigma}{dt}\right|_0\right)^{1/2}\left\{3\cdot\left(\frac{\left.\frac{d\sigma}{dt}\right|_{t_1}}{\left.\frac{d\sigma}{dt}\right|_0}\right)\left(\frac{b^2(t_1)}{b^2(0)}\right) - 1\right\} \qquad (13)$$

where

$$t = 3t_1\left(1 + \frac{t_1}{4k^2}\right)$$

k = center of mass momentum

$$b(t) = \frac{d\sigma}{dt}[\ln(d\sigma/dt)]$$

In Fig. 16 we plot the right-hand side minus the left-hand side of Eq. 13. (For this study we parameterized the data by Eq. 10 with the quadratic form for the matrix element.) Figure 17 demonstrates that our data satisfy the bound, in contrast to the conclusions of Ref. 26.[27] It is interesting that the bound is not violated for the pp scattering data; Ref. 26 does not address nucleon-nucleon elastic scattering. Strictly speaking the data test the bound only for $-t > 0.075$ $(GeV/C)^2$. For $-t \gtrsim 0.25$ $(GeV/c)^2$ the right-hand side of Eq. 11 is negative, and the bound is not useful. At $t = t_1 = 0$ the two sides of the bound are by definition equal; thus at small t it is not surprising that the bound appears saturated. Finally it can be shown on general grounds that if dσ/dt is parameterized by Eq. 10 with an exponential matrix element (Eq. 11b) and u, r_p, and r_π are all greater than zero, then it is impossible to violate the bound at any t.[12]

CONCLUSION

We have measured $d\sigma/dt$ distributions for π^-p, π^+p, and pp elastic scattering in the range $0.021 < -t < 0.665$ $(GeV/c)^2$ and studied the shape of these distributions in detail. The variation of the local slope as a function of t is similar for π^+p and π^-p elastic scattering, while there are indications that the variation is different in pp elastic scattering.

Over the entire t range measured, $d\sigma/dt$ distributions for all three particles are inconsistent with the form of e^{bt}. However functional forms involving the product of the electromagnetic form factors of the projectile and the target and a simple matrix element adequately describe the data, especially for $-t < 0.32$ $(GeV/c)^2$. The AQM leads to such functional forms for the elastic cross sections. Within the context of this model we estimate the size of the clothed quark in the pion and proton.

Finally no violations of bounds on the elastic scattering amplitude were found.

ACKNOWLEDGEMENTS

We would like to thank the following people for their valuable contributions: Peter Martin, Satish Dhawan, Adrian Disco, Irving Winters, Jon Blomquist, Garvie Hale, and Ed Steigmeyer. We also thank William Frieze for his work on early parts of this experiment. This work was supported in part by the U.S. Department of Energy. One of us (L.R.) was a fellow of the Swiss National Fund for Scientific Research and a second member (L.A.F.) was supported

in part by a Ford Foundation Doctoral Fellowship for Mexican-Americans and Puerto Ricans.

We also thank A. Bialas and H. Miettenen for a number of stimulating discussions.

REFERENCES

[a]Present address: Bell Laboratories
Holmdel, New Jersey 07733

[b]Present address: Lawrence Berkeley Laboratory
Berkeley, California 94720

[c]Present Address: CERN, Geneva, Switzerland

[d]Visitor from: Rutherford Laboratory, Chilton,
Didcot, Berkshire, England

[e]Present address: SLAC, P.O. Box 4349
Stanford, CAlifornia 94035

[f]Present address: Brookhaven National Laboratory
Upton, New York 11973

[g]Present address: Arthur Young and Company
One IBM Plaza, Chicago, Illinois 60611

[1]G. Giacomelli, Phys. Rep. 23C, 123 (1976); Istituto di Fisica dell'Universita di Bologna Preprint IFUB 77-12 (1977).

[2]D. S. Ayres et al., Phys. Rev. D15, 3105 (1977); Fermilab SAS, Phys. Rev. Lett. 37, 548 (1976).

[3]C. W. Akerlof et al., Phys. Rev. D14, 2864 (1976).

[4]R. K. Carnegie et al., Phys. Lett. 59B, 313 (1975).

[5]G. Barbiellini et al., Phys. Lett. 39B, 663 (1972).

[6]J. P. Burq et al., CERN EP Internal Report 78-7, 12/14178.

[7]J. R. Orr and A. L. Read, Meson Laboratory, Preliminary Design Report, March 1971, Fermilab.

[8]A.J. Slaughter et al., "A High Resolution Spectrometer for a Small Angle Scattering Experiment at Fermilab", to be published.

[9]S. Dhawan and R. Majka, "A Hardware Scatter Detector", IEEE Transactions on Nuclear Science, Vol. NS-22 (1975).

[10]Digitial Equipment Corp., Maynard, Massachusetts.

[11]M. Sogard, Phys. Rev. D9, 1486 (1974).

[12]"Hadron-Nucleus Elastic Scattering at 70, 125, and 175 GeV/c and a High Statistics Study of Hadron Proton Elastic Scattering at 200 GeV/c", A. Schiz, to be submitted as thesis, Yale University.

[13]F. James and M. Roos, CERN Computer 7600 Interim Program Library, D506 and D516.

[14]F. Jenkins et al., Fermilab-PUB-78/35-EXP, submitted to Sov. J. Nucl. Phys.

[15]V. Bartenev et al., Phys. Rev. Lett. 31, 1088 (1973).

[16]R. Schamberger, Jr. et. al., Phys. Rev. D17, 1268 (1978).

[17]G. Bohler et al., Institut fur Theoretische Kernphysik Preprint, TKP 79-4, June, 1979.

[18]T. T. Chou and C. N. Yang, Phys. Rev. 170, 1591 (1968).

[19]A. Bialas et al., Acta Phys. Pol. B8, 855 (1977); N. W. Dean, Phys. Rev. 1D, 2703 (1970).

[20]H.J. Lipkin et al., Phys. Rev. 152, 1375(1966); J. J. J. Kokkedee and L. Van Hove, Nuovo Cim. 42, 711 (1966); E. M. Levin and V. M. Shekhter, Leningrad Nuclear Physics Institute Preprint, "Small-Angle Elastic Scattering and Quark Model", 1978; E. M. Levin and V. M. Shekhter, Proc. of the IXth Winter LNPI School on Nuclear Physics and Elementary Particles (Leningrad 1974), Vol. III.

[21]The quark-quark scattering amplitude is written in impact parameter space (b-space) as exp (b^2/r_q^2), private communication, H. Miettinen. A similar parameterization is used in reference 19.

[22]D. A. Andrews et al., J. Phys. G.: Nucl. Phys. 3, L91 (1977) and reference therein

[23]A. Quenzer et atl., Phys. Lett. 76B, 512 (1978) and references therein.

[24]V. Singh and S. M. Roy, Phys. Rev. Lett. 24, 28 (1970). For more detail, see V. Singh and S. M. Roy, Phys. Rev. 1D, 2638 (1970).

[25]S. M. Roy, Phys. Rep. 5C, 125 (1972).

[26]S. M. Roy, Phys. Rev. Lett. 43, 19 (1979).

[27]See also G. Höhler et al., Institut fur Theoretische Kernphysik Preprint, TKP 79.8, July 1979.

Table I

Major Cuts to Extract Elastic Signal

	Cut	Fractions of Events Remaining After Cut		
		π^-	π^+	p
1)	Track reconstruction requirements on PWC coordinates · HFD test passed	.446	.545	.546
2)	No count from VH2 and VH3	.368	.457	.447
3)	HSD Test Passed	.366	.455	.447
4)	Scattering angle in x and y projections $\geq$.25 mrad	.355	.444	.443
5)	Track $\leq$ 1.5 cm from center of PWC station 4.	.352	.438	.440
6)	Outgoing particle trajectory traversed the area inside of spectometer magnet apertures	.342	.427	.430
7)	Scatter vertex no more than 40cm beyond LH_2 target ends	.293	.361	.375
8)	$0.0 \leq$ Recoil Mass Squared $\leq$ 1.76 $(GeV/c^2)^2$	.215	.272	.287
9)	Events whose trajectories were in region of > 90% efficiency in PWC station 4.	.167	.254	.269
10)	Outgoing particle trajectory did not traverse the area of the counter V at the third focus.	.120	.217	.231

TABLE II

Tabulation of differential cross sections. Errors are statistical only. Coulomb scattering contributions have been subtracted, and corrections for radiative effects, inelastic contamination, and plural nuclear scattering are included.

$\pi^- p$ 200 GeV/c

$-t$ (GeV/c)^2	$d\sigma/dt$ [mb/(GeV/c)^2]	
.0206	25.38	± .47
.0221	24.52	± .47
.0236	24.33	± .45
.0252	24.17	± .44
.0268	23.90	± .43
.0285	22.70	± .41
.0302	22.57	± .41
.0320	21.74	± .39
.0338	21.81	± .38
.0357	21.75	± .39
.0377	20.55	± .37
.0396	19.69	± .35
.0417	20.58	± .37
.0438	19.76	± .36
.0459	19.10	± .35
.0481	19.11	± .35
.0503	18.78	± .34
.0526	18.48	± .33
.0549	18.10	± .34
.0573	17.51	± .33
.0598	16.86	± .31
.0622	16.45	± .31
.0648	15.96	± .30
.0674	15.72	± .30
.0700	15.58	± .29
.0727	14.90	± .29
.0755	14.84	± .28
.0782	14.42	± .27
.0811	14.28	± .27
.0840	13.03	± .25
.0869	14.04	± .27
.0899	12.34	± .24
.0930	12.94	± .25
.0961	12.05	± .24

$-t$ $(GeV/c)^2$	$d\sigma/dt$ $[mb/(GeV/c)^2]$		
.0992	11.77	±	.24
.1024	11.04	±	.22
.1057	11.07	±	.23
.1090	10.51	±	.21
.1123	10.13	±	.21
.1157	10.08	±	.21
.1192	9.48	±	.20
.1227	9.11	±	.19
.1263	9.39	±	.20
.1299	9.03	±	.19
.1335	8.64	±	.19
.1372	8.44	±	.18
.1410	7.84	±	.17
.1448	7.53	±	.17
.1487	7.43	±	.16
.1526	7.12	±	.16
.1565	6.82	±	.15
.1605	6.66	±	.14
.1646	6.22	±	.14
.1687	6.17	±	.14
.1729	6.19	±	.14
.1771	5.94	±	.14
.1814	5.74	±	.13
.1857	5.37	±	.12
.1901	5.08	±	.12
.1945	4.85	±	.12
.1990	4.90	±	.12
.2035	4.63	±	.11
.2081	4.42	±	.11
.2127	4.33	±	.11
.2173	4.22	±	.11
.2221	4.14	±	.10
.2268	3.89	±	.10
.2317	3.54	±	.09
.2366	3.55	±	.10
.2415	3.46	±	.09
.2465	3.17	±	.09
.2515	3.02	±	.08
.2566	3.08	±	.08
.2617	2.88	±	.08
.2669	2.82	±	.08
.2721	2.82	±	.08
.2774	2.61	±	.08
.2827	2.59	±	.07
.2881	2.51	±	.07
.2936	2.24	±	.07
.2990	2.12	±	.06
.3046	2.13	±	.06
.3102	1.98	±	.06
.3158	1.98	±	.06
.3215	1.85	±	.06

$-t$ (GeV/c)^2	$d\sigma/dt$ [mb/(GeV/c)^2]		
.3272	1.75	±	.06
.3330	1.55	±	.05
.3389	1.55	±	.05
.3448	1.49	±	.05
.3507	1.59	±	.05
.3567	1.42	±	.05
.3627	1.42	±	.05
.3688	1.30	±	.05
.3750	1.23	±	.04
.3812	1.21	±	.04
.3874	1.18	±	.04
.3937	1.04	±	.04
.4001	1.07	±	.04
.4065	.98	±	.04
.4129	.91	±	.04
.4194	.87	±	.04
.4260	.88	±	.04
.4326	.73	±	.04
.4393	.75	±	.03
.4460	.76	±	.03
.4527	.75	±	.03
.4595	.71	±	.03
.4664	.68	±	.03
.4733	.60	±	.04
.4803	.60	±	.03
.4873	.59	±	.03
.4943	.55	±	.03
.5014	.48	±	.03
.5086	.50	±	.03
.5158	.49	±	.03
.5231	.48	±	.03
.5304	.44	±	.03
.5378	.39	±	.03
.5452	.38	±	.02
.5526	.37	±	.02
.5602	.34	±	.02
.5677	.33	±	.02
.5754	.32	±	.02
.5830	.33	±	.02
.5909	.28	±	.02
.5985	.27	±	.02
.6063	.28	±	.02
.6142	.23	±	.03
.6221	.26	±	.02
.6301	.21	±	.02
.6382	.24	±	.03
.6462	.23	±	.02
.6544	.22	±	.02
.6625	.20	±	.02

$\pi^+ p$ 200 GeV/c

$-t$ (GeV/c)^2	$d\sigma/dt$ [mb/(GeV/c)^2]	
.0220	24.09	± .46
.0235	23.53	± .43
.0251	23.60	± .44
.0267	23.22	± .42
.0284	22.91	± .40
.0301	22.32	± .41
.0319	21.77	± .39
.0337	22.01	± .39
.0356	20.89	± .38
.0375	20.65	± .37
.0395	20.53	± .36
.0415	19.97	± .36
.0436	19.21	± .35
.0457	18.70	± .34
.0479	18.76	± .33
.0501	18.22	± .34
.0524	17.29	± .32
.0547	17.18	± .31
.0571	16.86	± .31
.0595	16.53	± .30
.0620	16.31	± .30
.0645	16.23	± .29
.0671	15.61	± .29
.0697	15.13	± .28
.0724	14.79	± .28
.0752	14.44	± .27
.0779	13.72	± .27
.0808	13.56	± .26
.0837	13.02	± .26
.0866	13.35	± .26
.0896	12.63	± .25
.0926	12.20	± .24
.0957	11.95	± .24
.0988	11.20	± .24
.1020	11.35	± .23
.1053	10.81	± .23
.1086	10.69	± .22
.1119	10.02	± .21
.1153	9.99	± .21
.1187	9.63	± .21
.1222	9.22	± .21
.1258	9.00	± .20
.1293	8.54	± .19
.1330	8.85	± .19
.1367	8.11	± .19
.1404	7.96	± .18

$-t$ (GeV/c)^2	$d\sigma/dt$ [mb/(GeV/c)^2]		
.1442	7.71	±	.18
.1481	7.15	±	.17
.1520	7.24	±	.18
.1559	6.96	±	.17
.1599	7.00	±	.16
.1640	6.38	±	.16
.1681	6.56	±	.16
.1722	5.81	±	.16
.1764	5.94	±	.15
.1807	5.74	±	.15
.1850	5.21	±	.14
.1893	5.35	±	.15
.1937	4.90	±	.14
.1982	4.91	±	.14
.2027	4.40	±	.12
.2072	4.37	±	.13
.2118	4.36	±	.13
.2165	4.11	±	.12
.2212	4.00	±	.11
.2259	3.67	±	.11
.2308	3.87	±	.11
.2356	3.44	±	.11
.2405	3.45	±	.11
.2455	3.21	±	.10
.2505	3.02	±	.10
.2556	2.97	±	.10
.2607	3.01	±	.10
.2658	2.81	±	.09
.2710	2.66	±	.09
.2763	2.54	±	.09
.2816	2.52	±	.09
.2870	2.43	±	.09
.2924	2.18	±	.08
.2979	2.14	±	.08
.3034	2.01	±	.08
.3089	2.08	±	.07
.3146	2.03	±	.07
.3202	1.77	±	.07
.3259	1.88	±	.07
.3317	1.68	±	.07
.3375	1.59	±	.06
.3434	1.57	±	.07
.3493	1.50	±	.07
.3553	1.38	±	.06
.3613	1.54	±	.06
.3674	1.36	±	.06
.3735	1.26	±	.06
.3797	1.17	±	.05
.3859	1.16	±	.05

$-t$ (GeV/c)^2	$d\sigma/dt$ [mb/(GeV/c)^2]
.3922	1.05 ± .06
.3985	1.09 ± .06
.4049	.96 ± .06
.4113	.99 ± .06
.4178	.95 ± .06
.4243	.86 ± .06
.4309	.79 ± .05
.4375	.78 ± .05
.4442	.77 ± .05
.4509	.75 ± .05
.4577	.74 ± .05
.4645	.73 ± .05
.4714	.59 ± .05
.4784	.60 ± .04
.4853	.57 ± .04
.4924	.60 ± .04
.4995	.47 ± .04
.5066	.48 ± .05
.5138	.51 ± .04
.5210	.41 ± .04
.5283	.41 ± .05
.5356	.46 ± .04
.5430	.39 ± .04
.5505	.29 ± .06
.5579	.41 ± .04
.5655	.41 ± .04
.5731	.30 ± .04
.5807	.35 ± .04
.5884	.33 ± .04
.5962	.32 ± .04
.6039	.26 ± .04
.6118	.28 ± .04
.6197	.29 ± .05
.6276	.13 ± .08
.6356	.23 ± .05
.6437	.19 ± .04
.6518	.18 ± .05
.6599	.16 ± .05

pp 200 GeV/c

$-t$ (GeV/c)^2	$d\sigma/dt$ [mb/(GeV/c)^2]		
.0206	62.33	±	.60
.0220	61.36	±	.58
.0235	59.51	±	.57
.0251	58.80	±	.57
.0267	58.17	±	.56
.0284	57.01	±	.55
.0301	55.79	±	.54
.0319	54.82	±	.53
.0337	53.27	±	.52
.0356	52.49	±	.51
.0375	51.55	±	.50
.0395	49.61	±	.49
.0415	48.54	±	.48
.0436	47.11	±	.47
.0457	46.61	±	.46
.0479	45.46	±	.46
.0501	43.71	±	.44
.0524	42.26	±	.42
.0547	41.40	±	.42
.0571	40.46	±	.41
.0595	39.40	±	.41
.0620	38.57	±	.40
.0645	36.84	±	.38
.0671	35.87	±	.37
.0697	35.11	±	.37
.0724	33.59	±	.36
.0752	32.62	±	.35
.0779	31.70	±	.34
.0808	30.59	±	.33
.0837	29.56	±	.32
.0866	29.60	±	.32
.0896	27.93	±	.31
.0926	26.78	±	.30
.0957	26.10	±	.29
.0988	24.71	±	.28
.1020	24.54	±	.28
.1053	23.74	±	.27
.1086	22.57	±	.26
.1119	22.19	±	.26
.1153	20.69	±	.25
.1187	20.11	±	.24
.1222	19.57	±	.24
.1258	18.53	±	.23
.1293	17.88	±	.22
.1330	17.09	±	.21
.1367	16.64	±	.21
.1404	16.14	±	.20

$-t$ $(GeV/c)^2$	$d\sigma/dt$ $[mb/(GeV/c)^2]$		
.1442	15.53	±	.20
.1481	14.92	±	.19
.1520	14.50	±	.19
.1559	13.49	±	.18
.1599	13.03	±	.17
.1640	12.19	±	.17
.1681	11.94	±	.17
.1722	11.34	±	.16
.1764	10.92	±	.16
.1807	10.49	±	.15
.1850	10.03	±	.14
.1893	9.71	±	.14
.1937	9.02	±	.14
.1982	8.80	±	.13
.2027	8.49	±	.13
.2072	8.13	±	.12
.2118	7.54	±	.12
.2165	7.18	±	.11
.2212	6.65	±	.11
.2259	6.58	±	.10
.2308	6.24	±	.10
.2356	5.98	±	.10
.2405	5.85	±	.10
.2455	5.39	±	.09
.2505	5.18	±	.09
.2556	4.76	±	.09
.2607	4.48	±	.08
.2658	4.35	±	.08
.2710	4.28	±	.08
.2763	3.79	±	.07
.2816	3.70	±	.07
.2870	3.66	±	.07
.2924	3.41	±	.07
.2979	3.19	±	.06
.3034	3.19	±	.06
.3089	2.84	±	.06
.3146	2.79	±	.06
.3202	2.62	±	.06
.3259	2.56	±	.06
.3317	2.32	±	.05
.3375	2.23	±	.05
.3434	2.13	±	.05
.3493	2.00	±	.05
.3553	1.87	±	.05
.3613	1.86	±	.05
.3674	1.71	±	.05
.3735	1.62	±	.04
.3797	1.39	±	.04
.3859	1.41	±	.04

$-t$ $(GeV/c)^2$	$d\sigma/dt$ $[mb/(GeV/c)^2]$
.3922	1.35 ± .04
.3985	1.32 ± .04
.4049	1.25 ± .04
.4113	1.12 ± .03
.4178	1.09 ± .04
.4243	.99 ± .03
.4309	.93 ± .03
.4375	.93 ± .03
.4442	.86 ± .03
.4509	.83 ± .03
.4577	.71 ± .03
.4645	.70 ± .03
.4714	.68 ± .03
.4784	.60 ± .03
.4853	.57 ± .03
.4924	.55 ± .03
.4995	.49 ± .03
.5066	.47 ± .02
.5138	.43 ± .03
.5210	.45 ± .02
.5283	.37 ± .02
.5356	.37 ± .02
.5430	.39 ± .02
.5503	.32 ± .03
.5579	.32 ± .03
.5655	.27 ± .02
.5731	.25 ± .02
.5807	.22 ± .02
.5884	.19 ± .02
.5962	.22 ± .02
.6039	.24 ± .03
.6118	.21 ± .02
.6197	.16 ± .02
.6276	.18 ± .04
.6356	.14 ± .04
.6437	.13 ± .02
.6518	.14 ± .03
.6599	.12 ± .03

Table III

Parameters for Coulomb Scattering

Contribution to dσ/dt

$$\left.\frac{d\sigma}{dt}\right|^{\pm}_{coulomb} = \frac{4\pi\alpha^2}{\beta^2 t^2} \mp \sigma_{hp} e^{bt/2} \alpha\rho/\beta t$$

where α = fine structure constant

ρ = ratio of real to imaginary part of the scattering amplitude

σ_{hp} = total cross section for hadron-proton scattering

b = forward logarithmic nuclear slope

β = particle velocity/c

	$b(GeV/c)^{-2}$	$\sigma_{hp}(mb)$[a]	ρ[b]
$p-p$	12.0	38.97	-.01
π^+-p	10.5	23.84	.04
π^--p	10.5	24.33	.08

[a] From A. S. Carroll et al., Phys. Rev. Lett. 33, 928 and 932 (1974)

[b] From R. D. Hendrick and B. Lautrup, Phys. Rev. D11, 529 (1975)

TABLE IV

Local Slope Values and Correlations

$\pi^- p$ 200 GeV/c

Local Slope	$\lvert t \rvert$ Range $(GeV/c)^2$	Value[a] $(GeV/c)^{-2}$
b_1	.022-.036	10.91 ± .55 (.25)
b_2	.036-.062	9.30 ± .29 (.18)
b_3	.062-.102	9.63 ± .23 (.17)
b_4	.102-.161	9.18 ± .17 (.10)
b_5	.161-.252	8.26 ± .11 (.08)
b_6	.252-.327	7.62 ± .16 (.18)
b_7	.327-.400	7.41 ± .24 (.22)
b_8	.400-.494	6.92 ± .27 (.23)
b_9	.494-.583	6.60 ± .49 (.43)

$\chi^2/DOF = 130.4/113$

Correlation Coefficients, $\rho_{b_i b_j}$[b]

	b_1	b_2	b_3	b_4	b_5	b_6	b_7	b_8
b_2	-.499							
b_3	.020	-.511						
b_4	-.102	.391	-.770					
b_5	.231	-.676	.472	-.591				
b_6	-.238	.674	-.355	.039	-.388			
b_7	.147	-.413	.200	.058	-.135	-.507		
b_8	-.067	.187	-.088	-.037	.110	.016	-.565	
b_9	.024	-.068	.032	.015	-.045	.018	.116	-.565

[a] Systematic error contributuion in parenthesis.

[b] $\rho_{b_i b_j} \equiv \sigma^2_{b_i b_j} / \sigma_{b_i} \sigma_{b_j}$. $\sigma_{b_i b_j}$ is the covariance between the quantities b_i and b_j; σ_{b_i} is the standard deviation of b_i.

$\pi^+ p$ 200 GeV/c

Local Slope	$\lvert t \rvert$ Range $(GeV/c)^2$	Value[a] $(GeV/c)^{-2}$
b_1	.024-.044	10.83 ± .63 (.32)
b_2	.044-.072	9.33 ± .33 (.19)
b_3	.072-.105	9.41 ± .31 (.17)
b_4	.105-.144	8.83 ± .33 (.18)
b_5	.144-.181	8.56 ± .33 (.21)
b_6	.181-.241	8.64 ± .20 (.30)
b_7	.241-.309	7.48 ± .24 (.25)
b_8	.309-.374	7.26 ± .34 (.34)
b_9	.374-.478	7.22 ± .30 (.33)
b_{10}	.478-.604	5.96 ± .50 (.42)

χ^2/DOF = 99.1/114

Correlation Coefficients, $\rho_{b_i b_j}$[b]

	b_1	b_2	b_3	b_4	b_5	b_6	b_7	b_8	b_9
b_2	-.673								
b_3	.183	-.503							
b_4	-.029	.182	-.713						
b_5	-.025	-.379	.533	-.703					
b_6	.046	.476	-.514	.119	-.382				
b_7	-.030	-.296	.305	-.003	-.187	-.404			
b_8	.015	.142	-.145	-.008	.146	-.065	-.558		
b_9	-.006	-.054	.055	.004	-.063	.060	.083	-.582	
b_{10}	.002	.016	-.017	-.001	.020	-.022	-.013	-.124	-.523

[a] Systematic error contribution in parenthesis.

[b] $\rho_{b_i b_j} \equiv \sigma^2_{b_i b_j} / \sigma_{b_i} \sigma_{b_j}$. $\sigma_{b_i b_j}$ is the covariance between the quantities b_i and b_j; σ_{b_i} is the standard deviation of b_i.

pp 200 GeV/c

Local Slope	$\|t\|$ Range $(GeV/c)^2$	Value[a] $(GeV/c)^{-2}$
b_1	.025-.055	12.07 ± .10 (.16)
b_2	.055-.084	11.53 ± .12 (.08)
b_3	.084-.109	11.12 ± .12 (.10)
b_4	.109-.152	10.71 ± .11 (.08)
b_5	.152-.194	10.64 ± .18 (.08)
b_6	.194-.246	10.38 ± .18 (.20)
b_7	.246-.315	9.72 ± .15 (.13)
b_8	.315-.424	9.34 ± .13 (.19)
b_9	.424-.528	9.48 ± .24 (.19)
b_{10}	.528-.644	9.35 ± .61 (.42)

$\chi^2/DOF = 115.1/116$

Correlation Coefficients, $\rho^{b}_{b_i b_j}$

	b_1	b_2	b_3	b_4	b_5	b_6	b_7	b_8	b_9
b_2	.211								
b_3	-.454	-.180							
b_4	-.355	-.644	.110						
b_5	.204	.221	-.316	-.559					
b_6	.036	.044	-.162	.252	-.675				
b_7	-.160	-.151	.410	-.287	.232	-.611			
b_8	.141	.131	-.348	.221	-.103	.126	-.558		
b_9	-.080	-.075	.198	-.123	.048	-.027	.122	-.530	
b_{10}	.032	.030	-.080	-.049	-.018	.005	-.021	.109	-.497

[a] Systematic error contribution in parenthesis.

[b] $\rho_{b_i b_j} \equiv \sigma^2_{b_i b_j} \sigma_{b_i} \sigma_{b_j}$. $\sigma_{b_i b_j}$ is the covariance between the quantities b_i and b_j; σ_{b_i} is the standard deviation of b_i.

Table V

Results from Fits of $d\sigma/dt$ to $e^{bt + ct^2}$

	$\|t\|$ Range	b	c	χ^2/DOF
p -p	.025 - .620	11.73 ± .04	-2.98 ± .10	186.0/125
π^+-p	.025 - .620	9.94 ± .07	-3.68 ± .16	106.0/125
π^--p	.025 - .620	9.88 ± .06	-3.43 ± .13	142.4/125

Table VI

Total Elastic Cross Sections

at 200 GeV/c

	$\sigma^{Elastic}_{(mb)}$	$\sigma^{Elastic}/\sigma^{Total}$[a]
$\pi^- p$	3.21 ± .15	.132 ± .006
$\pi^+ p$	3.08 ± .06	.129 ± .003
$p\ p$	6.82 ± .13	.175 ± .004

[a]From A. S. Carroll et. al., Phys. Rev. Lett. 33, 928 and 932 (1974)

TABLE VII

Results of fits of $R^{\pm}$ (as defined in text) to Ce^{dt}.

	$\lvert t \rvert$ Range	C	d	χ^2/DOF
R^+ (p/π^+)	.022-.630	2.67 ± .01	2.08 ± .06	126.1/128
R^- (p/π^-)	.022-.630	2.61 ± .01	1.98 ± .06	165.1/128

TABLE VIII

Results of Fits of dσ/dt to the Form Factor Parameterization with a Quadratic Matrix Element, Eqns. 10 and 11a

	$\|t\|$ Range $(GeV/c)^2$	A	u $(GeV/c)^{-2}$	r_π (fm)	r_p (fm)	χ^2/DOF
pp	0.025-0.620	79.32±.26	1.65±.03	—	.79±.01	124.9/122
π^+p	0.025-0.620	30.27±.19	1.01±.08	.61±.05	.86±.04	103.0/122
π^-p	0.025-0.620	30.88±.18	1.09±.07	.65±.04	.82±.03	136.1/122

TABLE IX

Results of Fits of dσ/dt to the Form Factor Parameterization with an Exponential Matrix Element, Eqns. 10, 11b, and 12

	$\|t\|$ Range $(GeV/c)^2$	A	r_q (fm)	r_π (fm)	r_p (fm)	χ^2/DOF
pp	0.025-0.620	78.40±.27	.51±.01	-	.71±.01	154.0/122
pp	0.025-0.320	79.27±.36	.46±.02	-	.75±.01	78.4/78
π^+p	0.025-0.620	30.18±.21	.34±.02	.65±.04	.79±.04	103.0/122
π^+p	0.025-0.320	30.11±.26	.36±.04	.63±.04	.78±.04	67.5/78
π^-p	0.025-0.620	30.78±.19	.40±.02	.70±.03	.72±.03	136.0/122
π^-p	0.025-0.320	30.91±.37	.31±.06	.61±.06	.84±.04	97.2/78

TABLE X

Results of Fits of $d\sigma/dt$ to Form Factor Parameterization
Using $\pi^- p$, $\pi^+ p$, pp Data Simultaneously[a]
$|A_{qq}|^2 = \exp(-r_q^2/2\hbar^2)$

$\|t\|$ Range	A_{π^-}	A_{π^+}	A_p	$r_q^{\pi^-}$ (fm)	$r_q^{\pi^+}$ (fm)	r_q^p (fm)	r_π (fm)	r_p (fm)	χ^2/DOF
0.025-0.620	30.63±.17	29.97±.16	80.19±.27	.37±.01	.37±.01	.43±.01	.65±.02	.77±.05	446.9/370
0.025-0.620[b]	29.89±.12	29.48±.12	80.31±.25	.42±.01	.42±.01	.42±.01	.55±.01	.77±.01	510.3/372
0.025-0.320	30.81±.25	30.25±.24	79.28±.37	.35±.03	.35±.03	.46±.02	.69±.03	.75±.01	243.8/238
0.025-0.320[b]	30.34±.15	29.87±.15	79.97±.31	.41±.01	.41±.01	.41±.01	.58±.01	.78±.01	257.6/240

a r_π, r_p each set to a single value for pion and proton data

b $r_q^{\pi^-}$, $r_q^{\pi^+}$, r_q^p constrained to be equal for pion and proton data

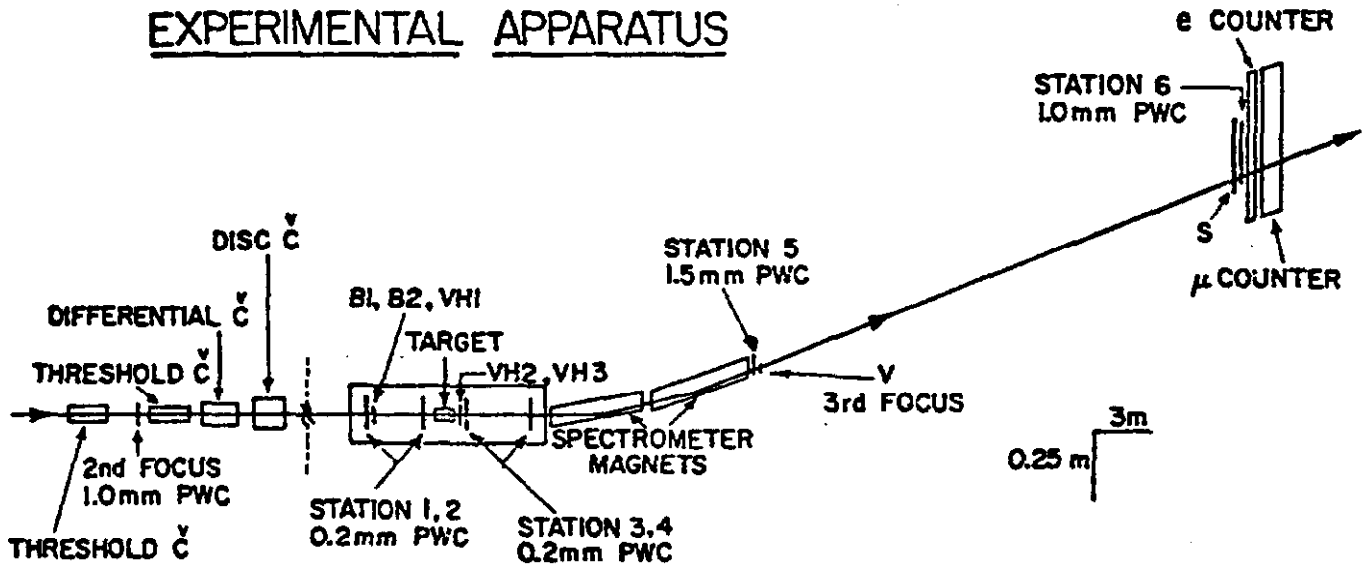

Figure 1: Experimental apparatus (not to scale left of vertical dashed line).

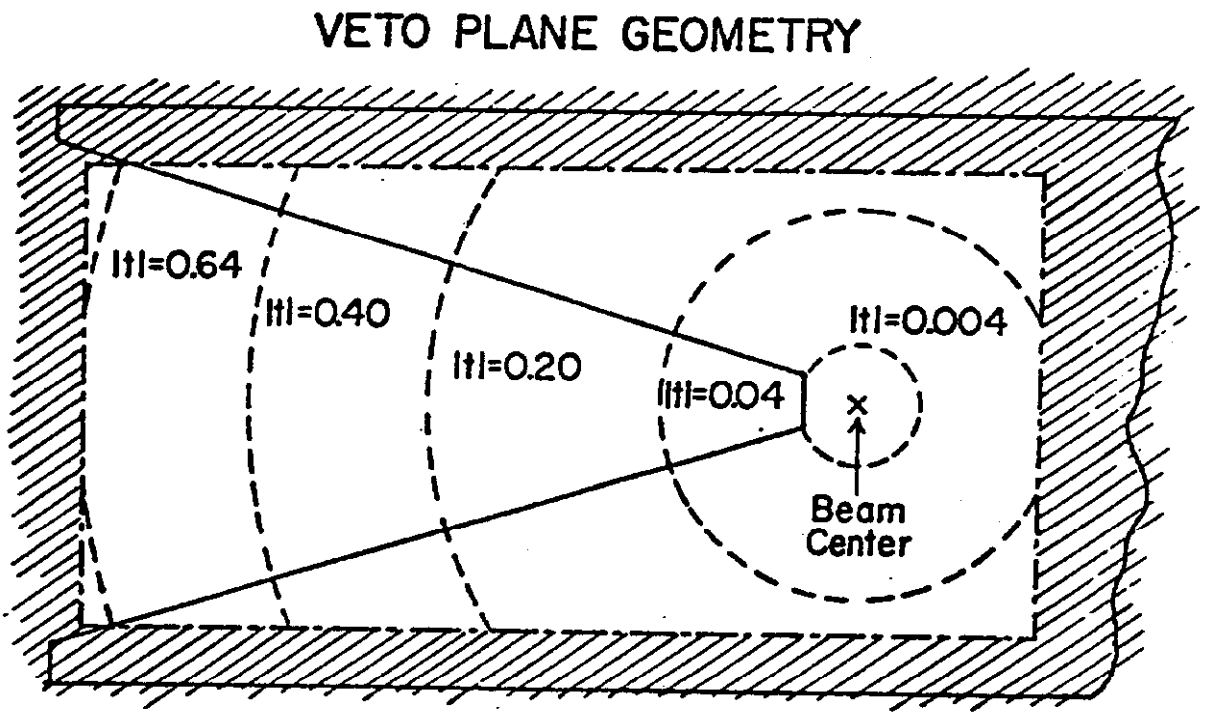

Figure 2: Veto plane geometry. The solid line denotes counter V, the shaded region denotes the projection of the downstream spectrometer magnet onto the veto plane. The dashed circles indicate the $|t|$ of a scattered particle originating on the beam center.

HFD and HSD Geometry

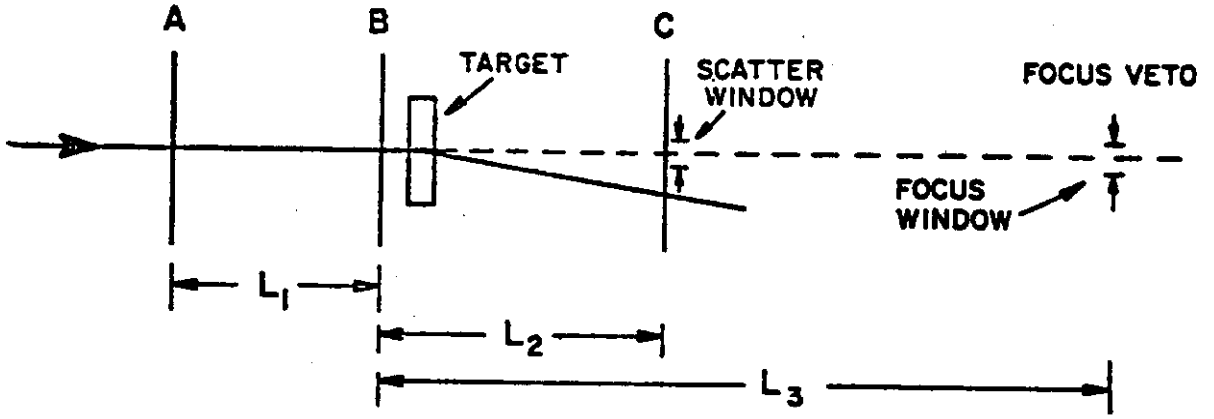

SCATTER: $\frac{L_2}{L_1} A + C - \left(\frac{L_1+L_2}{L_1}\right) B >$ Scatter Window

FOCUS: $\frac{L_3}{L_1} A - \left(1 + \frac{L_3}{L_1}\right) B <$ Focus Window

Fig. 3. Schematic presentation of HFSD operation.

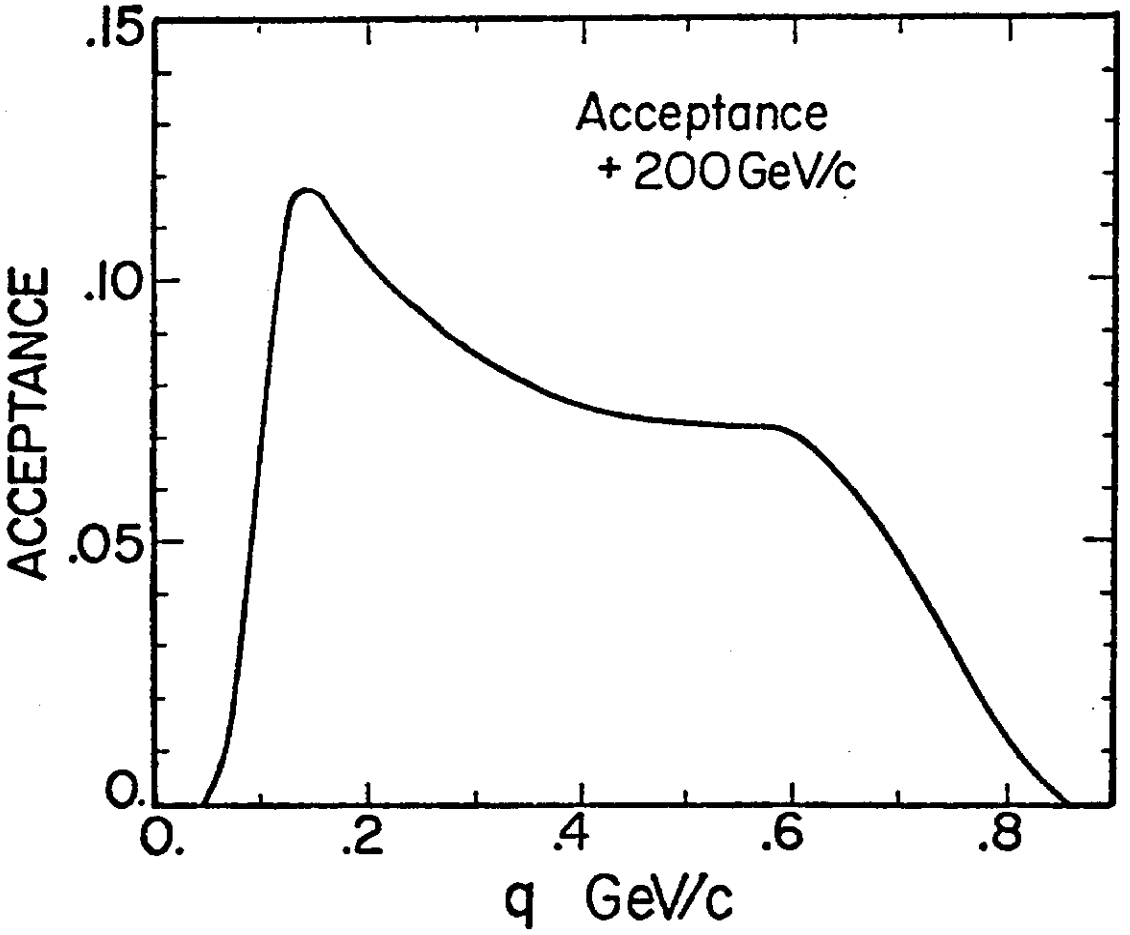

Fig. 4. Apparatus acceptance for $\pi^+ p$ and pp at 200 GeV/c.

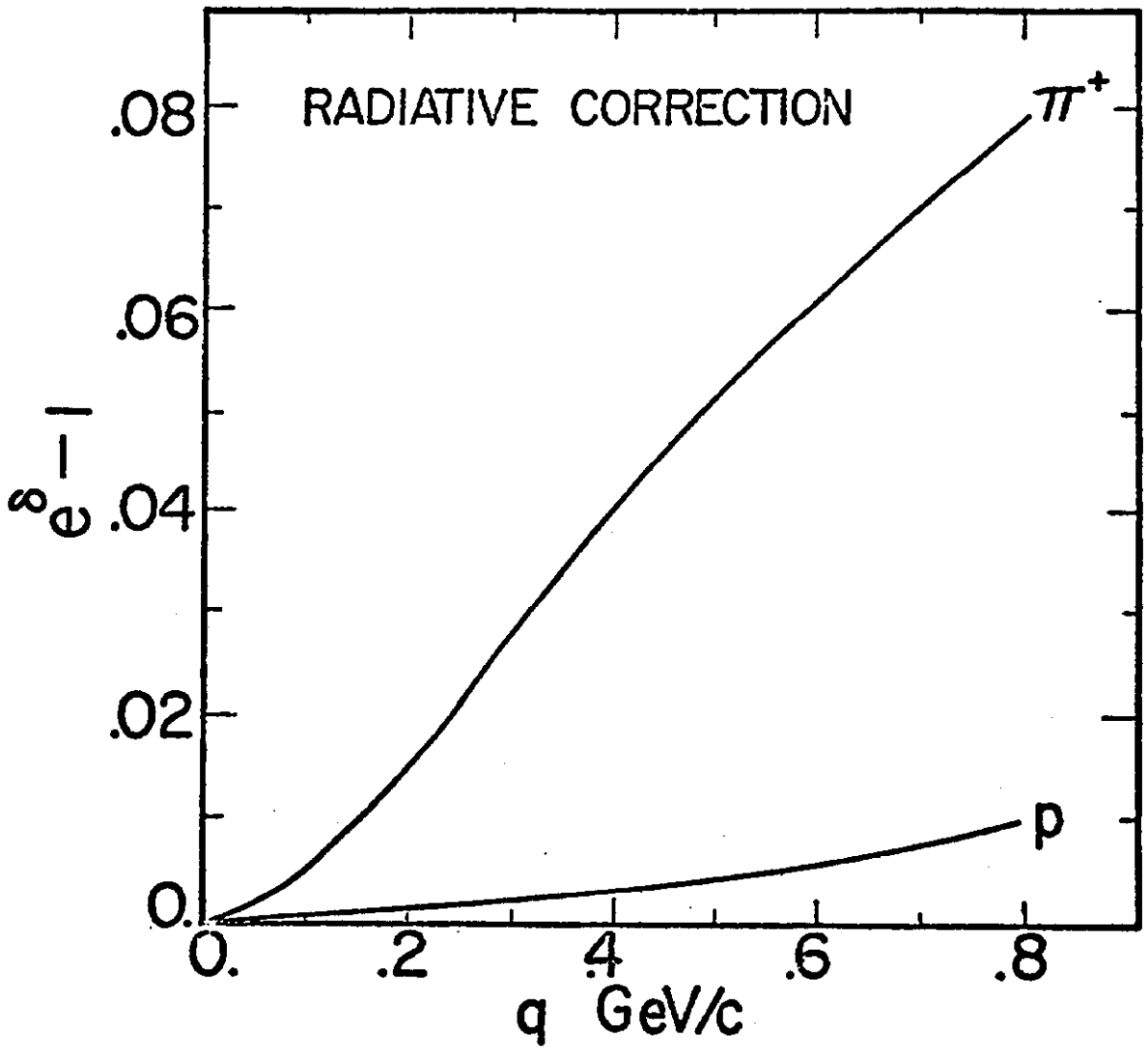

Figure 5: Correction for radiative effects. The data is corrected by e^{δ} (as explained in text).

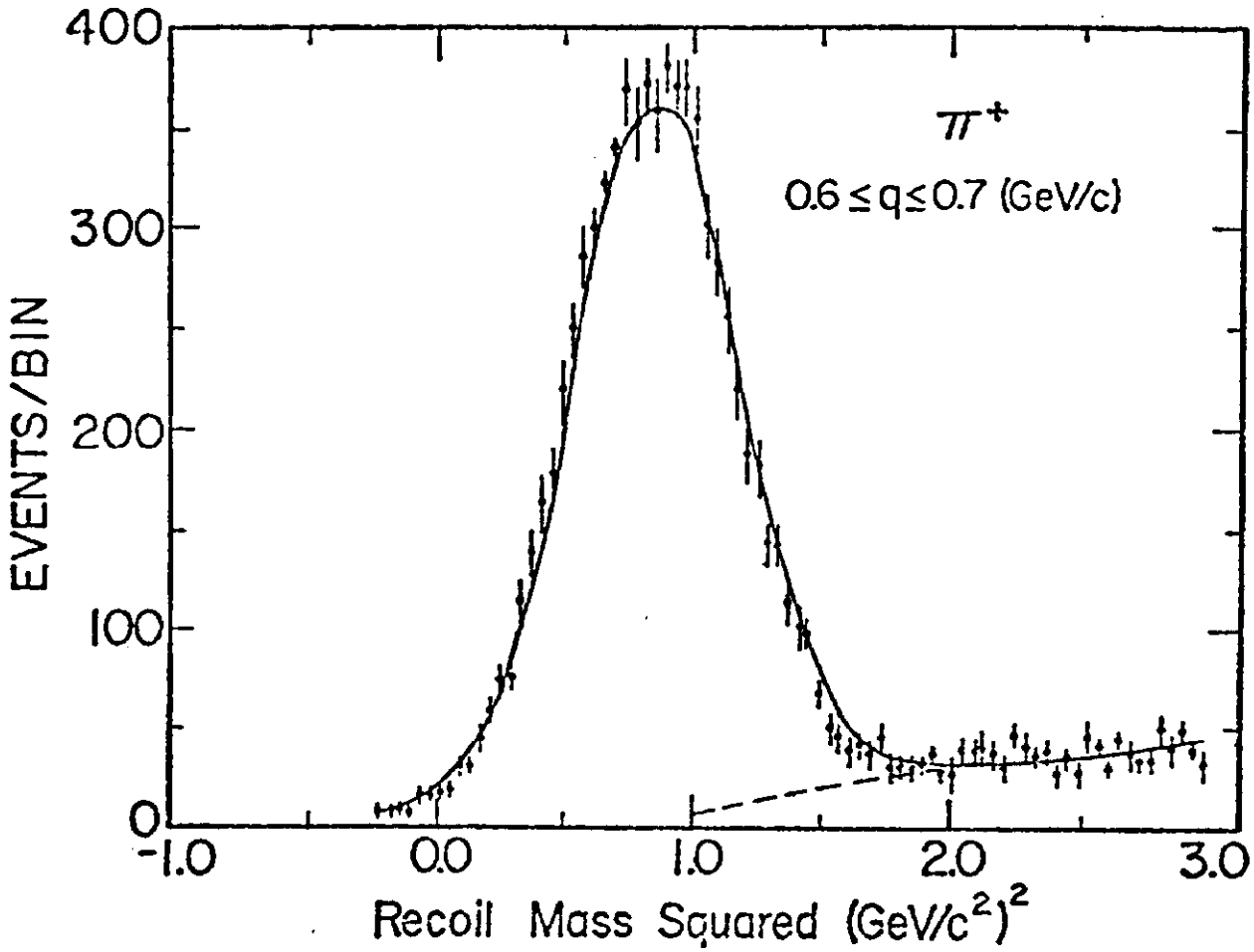

Figure 6: Result of a fit (solid line) used to calculate the amount of inelastic contamination. The specific case is for $\pi^+ p$ scattering for $0.05 \leq q \leq 0.07$ (GeV/c).

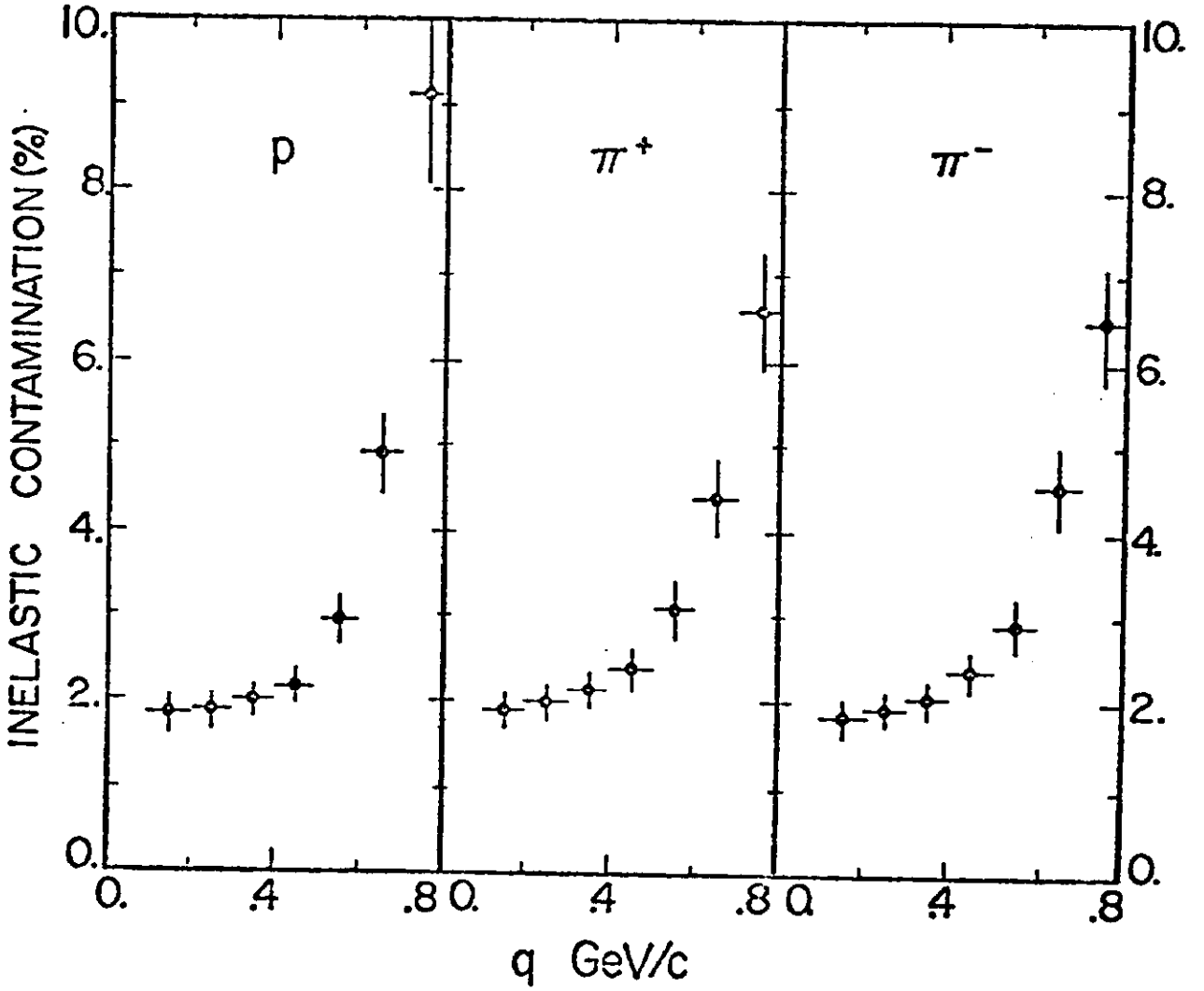

Figure 7: Inclastic contamination. The data is corrected as indicated in the text.

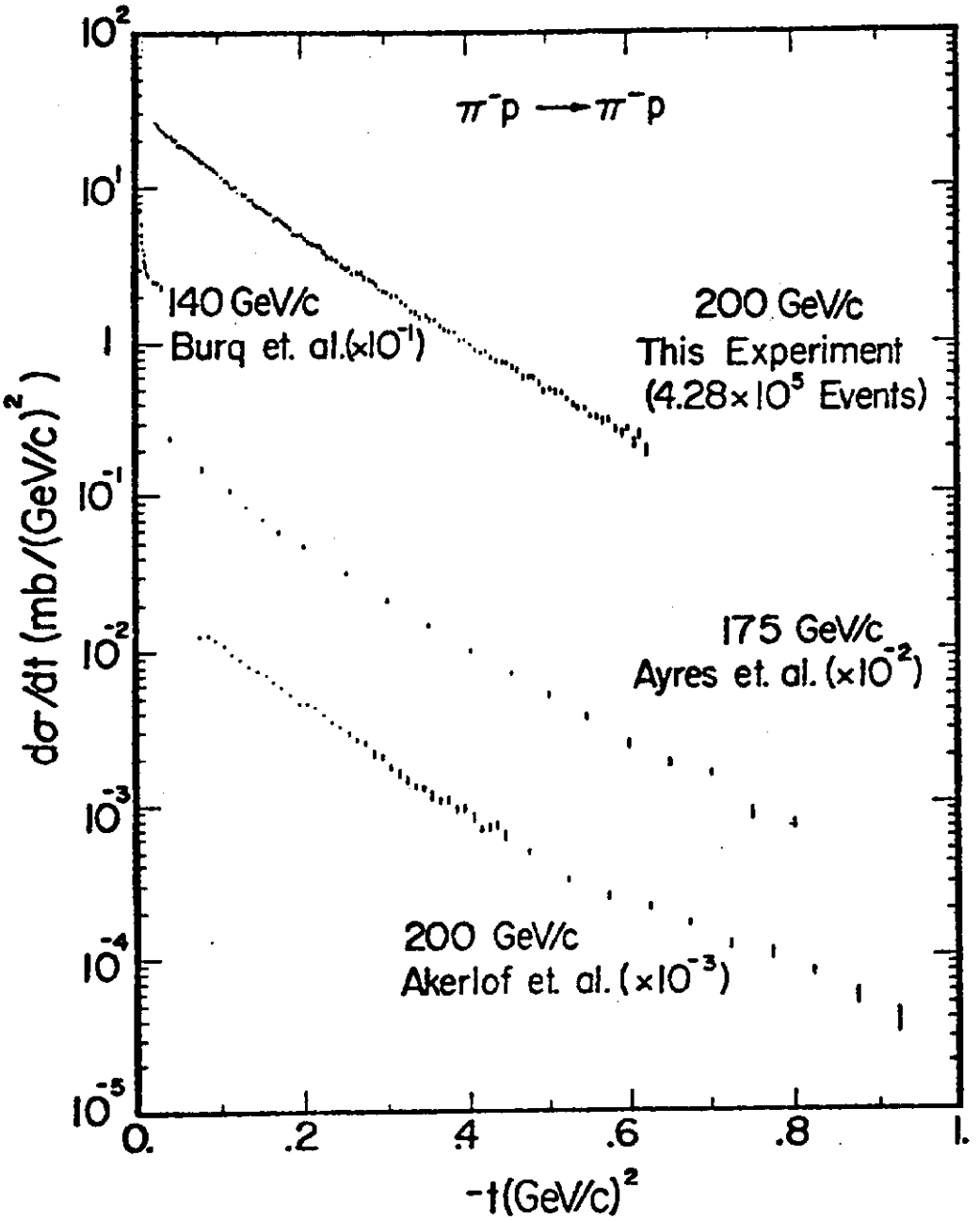

Figure 8: $d\sigma/dt$ for $\pi^- p$ elastic scattering as measured by this experiment (corrected for Coulomb scattering contributions, radiative effects, inelastic contamination, and plural nuclear scattering in the hydrogen target). Also shown are results from selected experiments. The data of Burq et al[6] include Coulomb scattering.

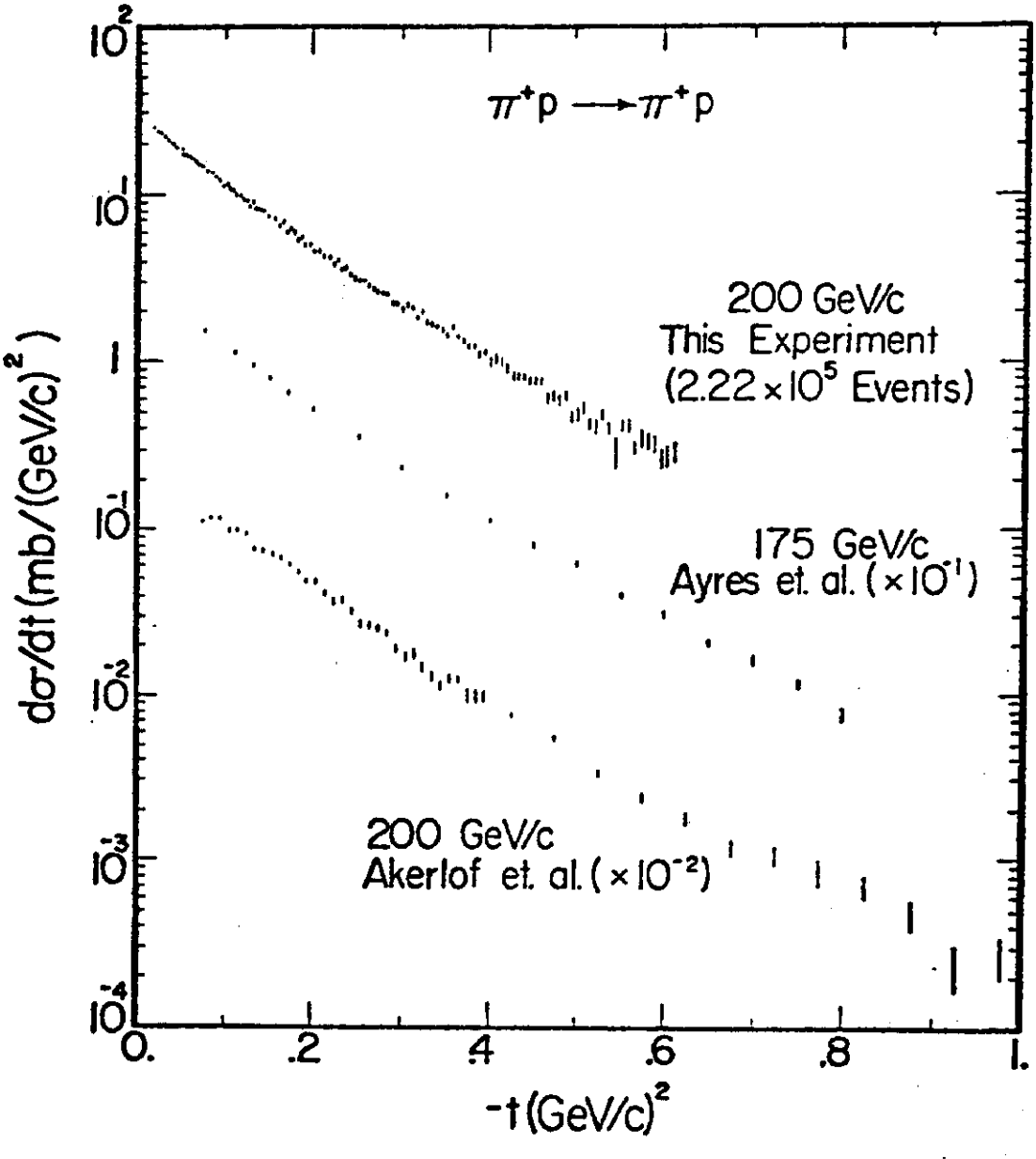

Figure 9: $d\sigma/dt$ for $\pi^+ p$ elastic scattering as measured by this experiment (corrected for Coulomb scattering contributions, radiative effects, inelastic contamination, and plural nuclear scattering in the hydrogen target). Also shown are results from selected experiments.

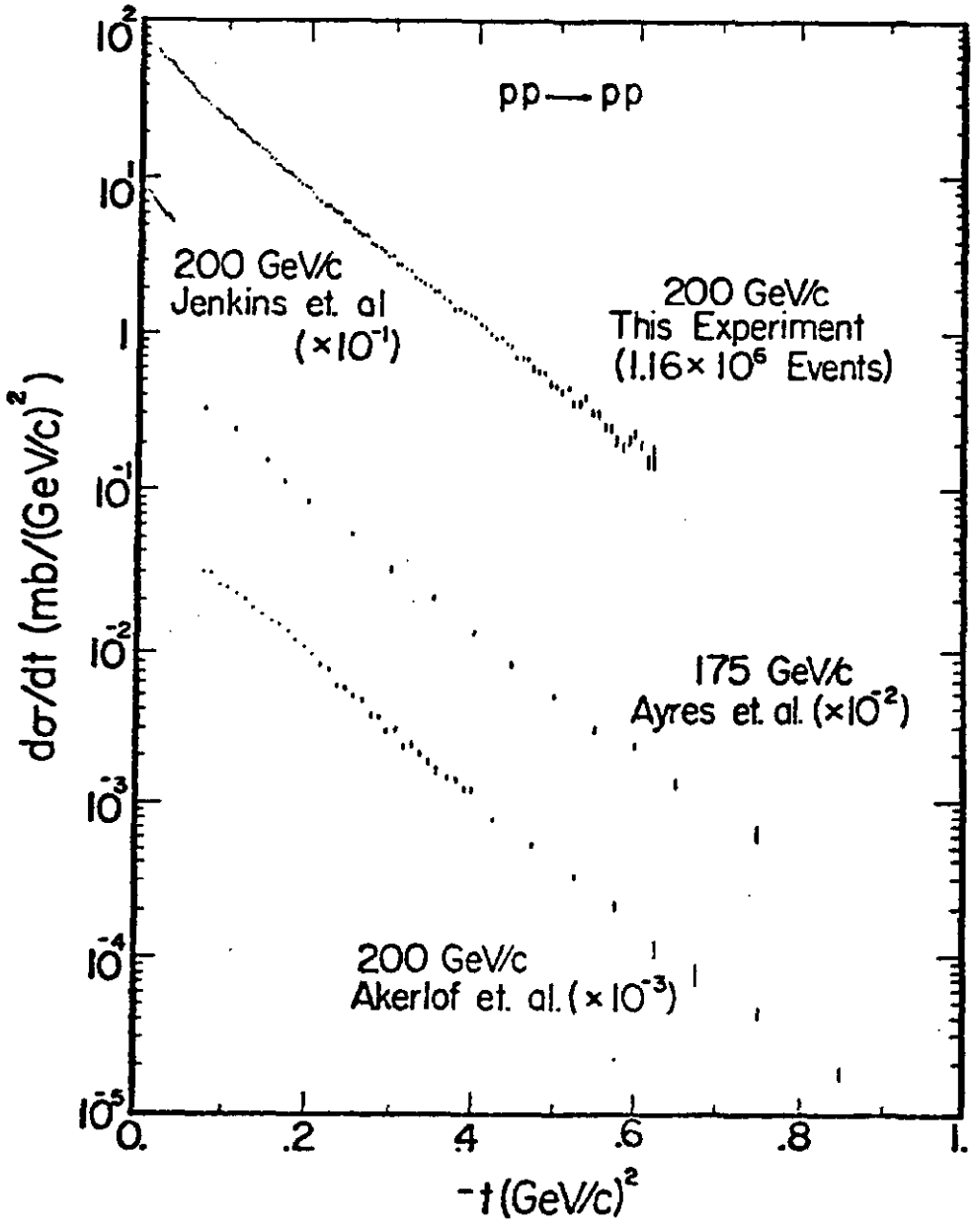

Figure 10: dσ/dt for elastic pp scattering as measured by this experiment (corrected for Coulomb scattering contributions, radiative effects, inelastic contamination and plural nuclear scattering in the hydrogen target). Also shown are results from selected experiments. The data of Jenkins et al[14] include Coulomb scattering.

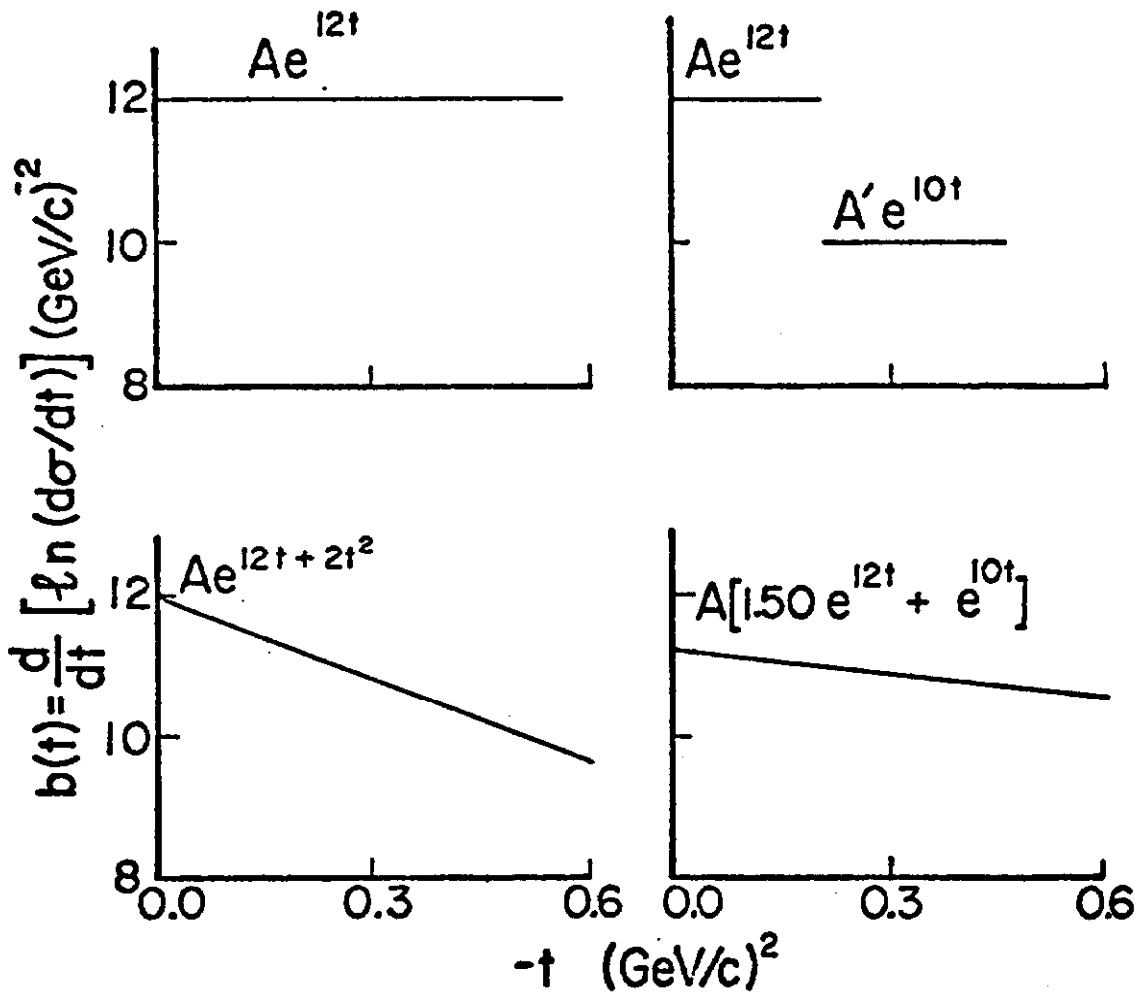

Figure 11: Local slope as a function of t for some representative shapes of dσ/dt.

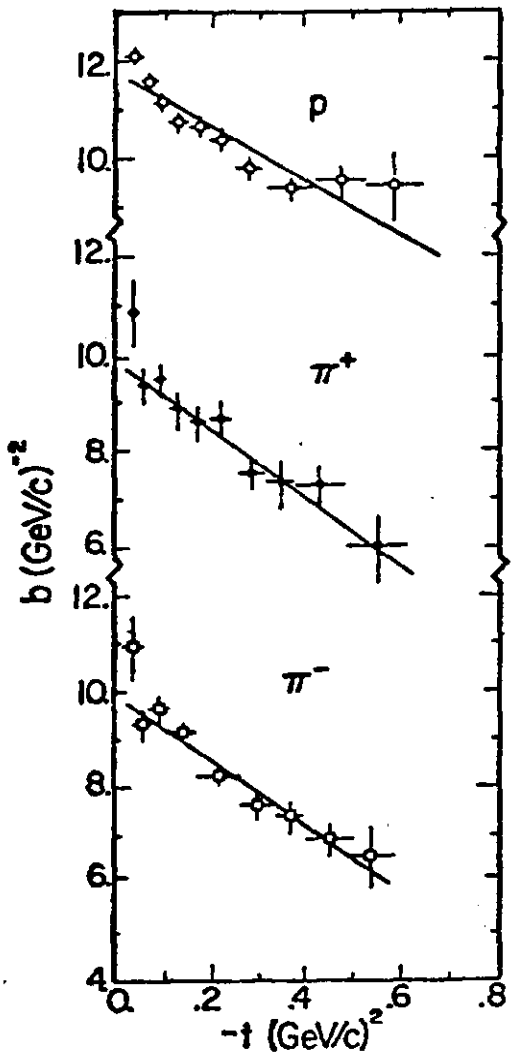

Figure 12: Local slope as a function of t for π^-p, π^+p, and pp elastic scattering. Errors include both statistical and systematic errors added in quadrature. Solid lines present local slope as calculated from fits of $d\sigma/dt$ to $\exp(bt+ct^2)$.

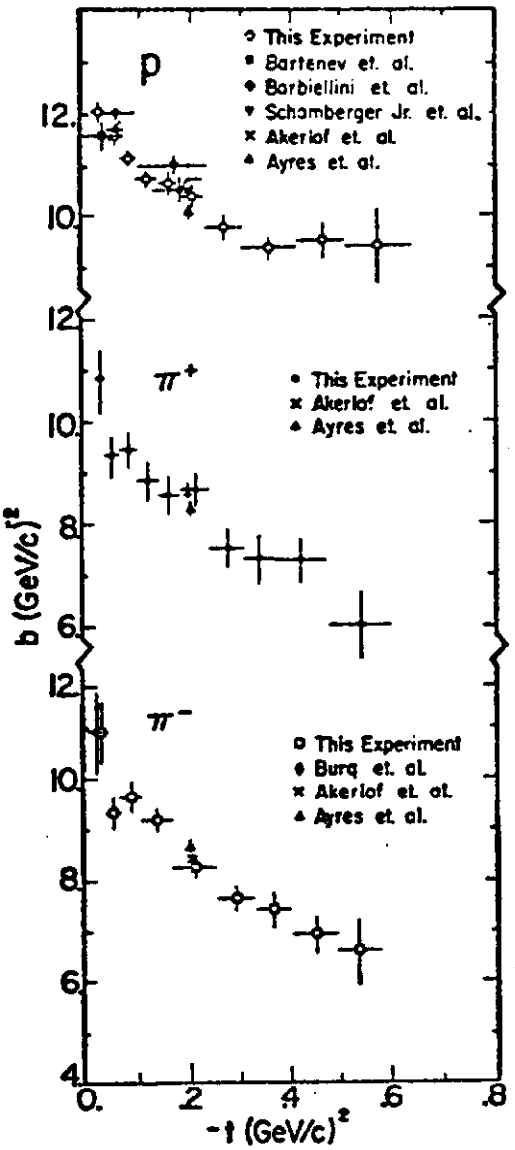

Figure 13: Comparison of measurements by several experiments of the logarithmic slope for $\pi^- p$, $\pi^+ p$, and pp elastic scattering.

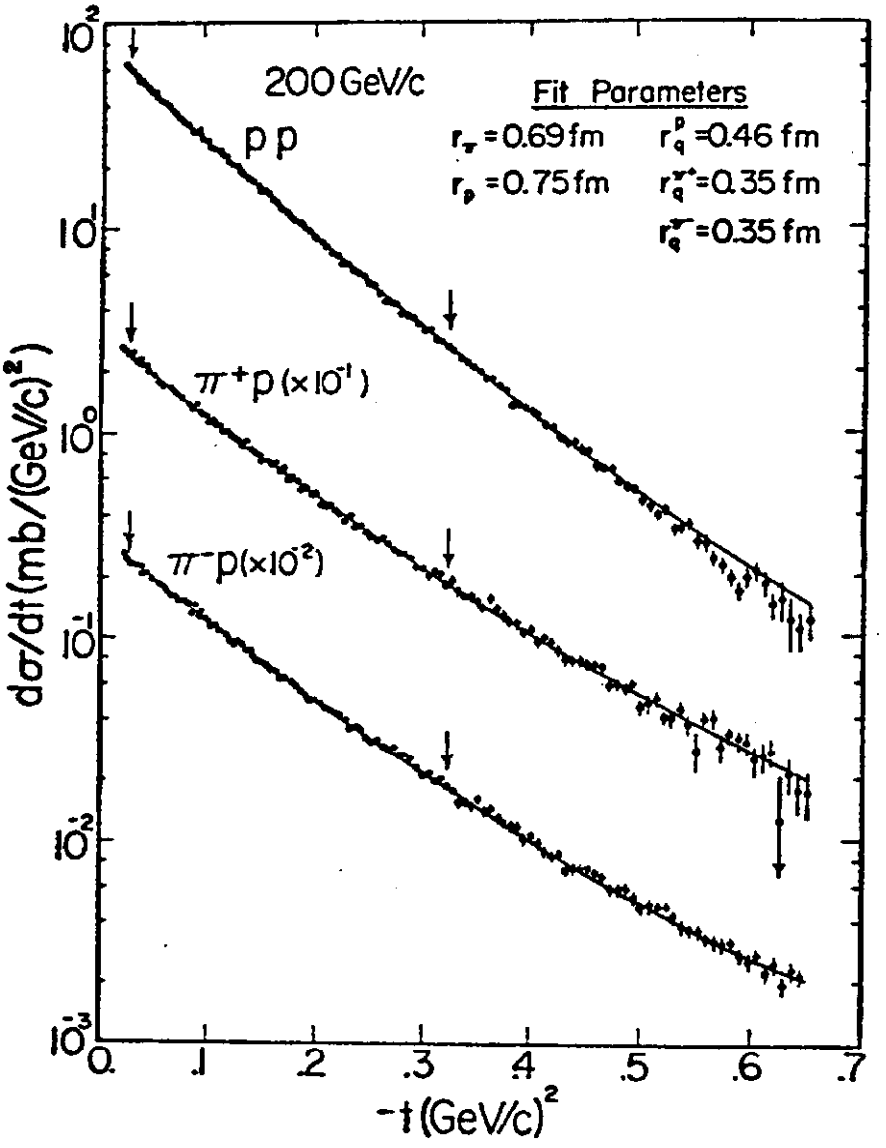

Figure 14: Results from fits to $\pi^- p$, $\pi^+ p$, and pp simultaneously using equations 10 and 11b. Arrows indicate the region of -t used in the fits.

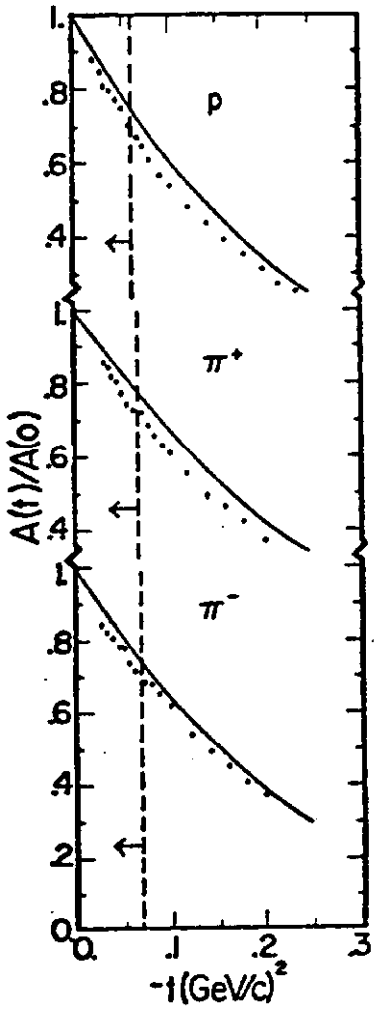

Figure 15: Comparison of representative results from this experiment (dots) with the upper limit on the ratio of the scattering amplitude at a given t to the scattering amplitude at t = 0, Eq. 13 of Ref. 24 (solid line). The upper limit holds rigorously only to the left of the dashed lines (as shown by the arrow).

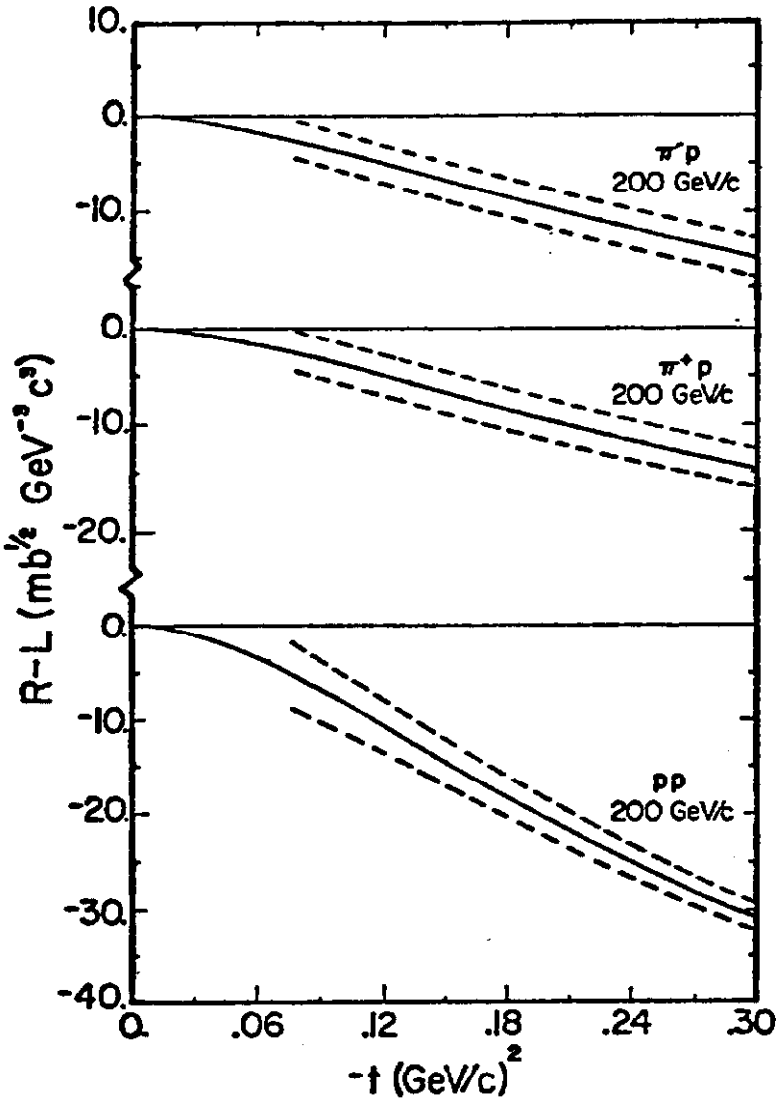

Figure 16: Right-hand side minus left-hand side of Eq. 13, R-L, (solid line). Dashed lines give ±1 standard deviation error band; error band shown only for $-t > 0.075$ (GeV/c)^2.